HOKKAIDO UNIVERSITY

Title	Eddy-Eddy and Eddy-Mean Flow Interactions in an Eastward Jet Flanked by Recirculation Gyres
Author(s)	Mizuta, Genta
Citation	Journal of physical oceanography, 56(5), 1103-1123 https://doi.org/10.1175/JPO-D-25-0062.1
Issue Date	2026-05-01
Doc URL	https://hdl.handle.net/2115/99447
Rights	© Copyright 2026 American Meteorological Society (AMS). For permission to reuse any portion of this Work, please contact permissions@ametsoc.org. Any use of material in this Work that is determined to be “fair use” under Section 107 of the U.S. Copyright Act (17 U.S. Code § 107) or that satisfies the conditions specified in Section 108 of the U.S. Copyright Act (17 USC § 108) does not require the AMS’s permission. Republication, systematic reproduction, posting in electronic form, such as on a website or in a searchable database, or other uses of this material, except as exempted by the above statement, requires written permission or a license from the AMS. All AMS journals and monograph publications are registered with the Copyright Clearance Center (https://www.copyright.com). Additional details are provided in the AMS Copyright Policy statement, available on the AMS website (https://www.ametsoc.org/PUBSCopyrightPolicy).
Type	journal article
File Information	phoc-JPO-D-25-0062.1.pdf

Hokkaido University Collection of Scholarly and Academic Papers : HUSCAP

Eddy–Eddy and Eddy–Mean Flow Interactions in an Eastward Jet Flanked by Recirculation Gyres

GENTA MIZUTA[a]

[a] *Graduate School of Environmental Earth Science, Hokkaido University, Sapporo, Japan*

(Manuscript received 14 March 2025, in final form 10 February 2026, accepted 27 February 2026)

ABSTRACT: To examine the role of the interaction of different eddies (eddy–eddy interaction) in driving recirculation gyres, we analyzed the budget of the eddy potential enstrophy (EE) in an eastward jet, dividing perturbations into different frequency bands. While the instability wave produced by jet instability is dominant in high-frequency bands, the Rossby wave radiated from the jet is dominant in low-frequency bands. The eddy potential vorticity (PV) flux is oriented in the upgradient direction of the mean PV in low-frequency bands, which is consistent with the PV flux generated by Rossby wave radiation. Although a large cancellation occurs between the changes in the EE by this upgradient PV flux and the advection of the EE, such cancellation is greatly reduced when the rotational component of the PV flux is subtracted. The change in the EE by the upgradient PV flux tends to be balanced by that produced by eddy–eddy interaction. The convergence of the upgradient PV flux balances with the change in the PV by the recirculation gyres, while the rotational component of the PV flux does not drive mean flows. Thus, it is strongly suggested that the Rossby wave is excited by eddy–eddy interaction and generates the upgradient PV flux, which drives the recirculation gyres. The substantial part of the EE is transferred from high- to low-frequency bands owing to this eddy–eddy interaction. The EE in high-frequency bands is supplied by jet instability in the upstream region of the jet and advected to the downstream region, where eddy–eddy interaction occurs. Thus, the EE produced by the jet instability contributes to exciting the Rossby wave.

KEYWORDS: Ocean; Ocean dynamics; Jets; Idealized models; Ocean models

1. Introduction

a. Recirculation gyres

The Gulf Stream in the North Atlantic and the Kuroshio and Kuroshio Extension in the North Pacific are major strong currents in the midlatitudes. These currents are part of the wind-driven circulation, which consists of the broad and weak Sverdrup flow in the ocean interior and the narrow and strong western boundary currents. After separating from the coast, the Gulf Stream and the Kuroshio Extension flow eastward in the middle of the ocean. These eastward jets are flanked by recirculation gyres that extend from the surface to the bottom on both sides (Kawai 1972; Worthington 1976; Hogg 1983, 1992; Jayne et al. 2009). The latitude and transport of the Kuroshio Extension and its recirculation gyres vary decadally (Qiu 2003; Qiu and Chen 2005; Taguchi et al. 2005, 2010) and affect the distribution of heat, freshwater, and biogeochemical materials (Qiu and Chen 2006, 2011; Oka et al. 2019).

Using an eddy-resolving numerical model, Holland and Rhines (1980) showed that the recirculation gyres are driven by eddies, which are themselves generated by the instability of the Gulf Stream and the Kuroshio. They showed that the recirculation gyres extend in both the surface and deep layers, which are forced by and isolated from the wind stress, respectively, because the recirculation gyres are essentially driven by eddies. To understand the mechanisms underlying the eddy–mean flow interaction, a number of analyses have been undertaken regarding the transfer of energy, momentum, and so forth (e.g., Chen et al. 2014; Berloff 2015; Aoki et al. 2016; Matsuta and Masumoto 2021). According to the numerical experiments conducted by Holland and Rhines (1980), the eddy potential vorticity (PV) flux, driving recirculation gyres, is not vertically uniform. While the eddy PV flux is oriented in the downgradient direction of the mean PV in the deep layer, the eddy PV flux is oriented in the upgradient direction of the mean PV in the surface layer except for a small region near the western boundary, where the eddy PV flux is oriented in the downgradient direction.

Two processes have been proposed as drivers of recirculation gyres. Rhines and Young (1982a,b) assumed that the downgradient eddy PV flux in the deep layer is expressed in the form of the Laplacian diffusion of the mean PV. Then, they showed that a weak diffusion of the PV drives significant mean circulation, in which the mean PV is homogeneous, in the lower layer of a two-layer quasigeostrophic model. This PV homogenization has also been proposed as a driver of recirculation gyres in the surface layer (Cessi et al. 1987; Jayne et al. 1996; Sheremet 2002). By using a simple barotropic model, Cessi et al. (1987) showed that the circulation similar to the southern recirculation gyre is formed when the PV is homogenized between the low PV fluid, which is advected from low latitudes by the western boundary currents, and the surrounding fluid. However, the assumption of the PV diffusion by Rhines and Young (1982a,b) is a priori. Although this assumption is consistent with the downgradient PV in the deep layer, the PV flux is oriented in the upgradient direction in most regions of the upper layer, and indeed the eddy diffusivity is mostly negative there (Holland and Rhines 1980).

The rectification of the Rossby wave energy radiated from the jet is another possible mechanism driving recirculation gyres (Thompson 1977; Hogg 1988; Malanotte-Rizzoli et al. 1995).

Corresponding author: Genta Mizuta, mizuta@ees.hokudai.ac.jp

DOI: 10.1175/JPO-D-25-0062.1

© 2026 American Meteorological Society. This published article is licensed under the terms of the default AMS reuse license. For information regarding reuse of this content and general copyright information, consult the AMS Copyright Policy (www.ametsoc.org/PUBSReuseLicenses).

Brought to you by HOKKAIDO DAIGAKU | Unauthenticated | Downloaded 05/13/26 12:03 AM UTC

TABLE 1. Experimental conditions.

Horizontal grid spacing, Δx, Δy (km)	10
Vertical grid spacing, Δz (m)	10–330
Bottom drag coefficient, r_b (m s^{-1})	4×10^{-5}
Vertical viscosity, ν_v (m^2 s^{-1})	5×10^{-2}
Vertical diffusivity, κ_v (m^2 s^{-1})	1×10^{-6}
Harmonic horizontal viscosity and diffusivity, ν_h, κ_h (m^2 s^{-1})	0
Biharmonic horizontal viscosity and diffusivity, ν_4, κ_4 (m^4 s^{-1})	0
Zonal and meridional width of the sponge layer, L_{sx}, L_{sy} (km)	200, 100

Conducting idealized numerical experiments with a barotropic quasigeostrophic model, in which the model was forced only by oscillatory forcing representing form drag, nonlinear interactions between different eddies (eddy–eddy interaction), and other effects, Haidvogel and Rhines (1983) demonstrated that the Rossby wave excited by oscillatory forcing drives a time-mean flow similar to the recirculation gyres. In contrast to the assumption of the PV diffusion, the PV flux in the forcing region of the Rossby wave is oriented in the upgradient direction of the mean PV, which agrees with the results of past numerical experiments for the surface layer (see above). Intense Rossby waves are often observed on the northern side of the Gulf Stream, with amplitudes of $O(0.1)$ m s^{-1} (Thompson 1977; Hogg 1988; Bower and Hogg 1992). Based on their numerical experiment of a forced eastward jet, Waterman and Jayne (2011) showed that the eddy PV flux is oriented in the upgradient direction of the mean PV in the region where the Rossby wave is radiated from the jet. They suggested that eddies produced by instability in the upstream region of the jet are transformed into the Rossby wave in the downstream region, generating this upgradient PV flux. However, the driving mechanism of recirculation gyres is not yet fully understood.

b. Enstrophy budget and eddy–eddy interaction

To understand the interaction between eddies and an eastward jet, Holland and Rhines (1980) and several studies have examined the budget of eddy potential enstrophy (EE; Rhines and Holland 1979; Marshall 1984; Wilson and Williams 2004; Waterman and Jayne 2011). The equation of the quasigeostrophic EE in the stationary state is expressed as

$$\overline{\mathbf{u}'q'} \cdot \nabla\overline{q} = -\overline{\mathbf{u}} \cdot \nabla\left(\frac{\overline{q'^2}}{2}\right) - \overline{q'\nabla \cdot (\mathbf{u}'q')} + \overline{D'q'}, \qquad (1)$$

where $\mathbf{u}$ is the horizontal velocity, q is the PV, ∇ is the horizontal gradient operator, and the overbar and prime denote the time average and perturbation from the average, respectively. The D' represents the arbitrary dissipation. The left-hand side of (1) represents the production/destruction of the EE by the downgradient/upgradient eddy PV flux (PUF). The first term on the right-hand side represents the advection of the EE by the mean flow, whereas the second term represents the eddy–eddy interaction, which is a third-order quantity in q' and $\mathbf{u}'$. The third term represents dissipation.

Assuming that the dissipation is negligible and the amplitude of the perturbation is small relative to the mean value, Holland and Rhines (1980) argued that the PUF in (1) is mainly balanced by the advection of the EE (i.e., the first term on the right-hand side) in the surface layer. In this case, the eddy PV flux has to be oriented in the upgradient direction in the region where the EE decreases in the downstream direction of the jet and vice versa. Thus, Holland and Rhines (1980) speculated that the PV flux was oriented in the upgradient direction in the surface layer of their experiment to achieve such a balance. Waterman and Jayne (2011) argued that the advection of the EE permits the upgradient PV flux, enhancing the Rossby wave radiation.

Of course, we cannot derive any causality solely from the term balance in (1) described above. Moreover, the eddy fluxes of PV, heat, and so forth maintained by such a balance

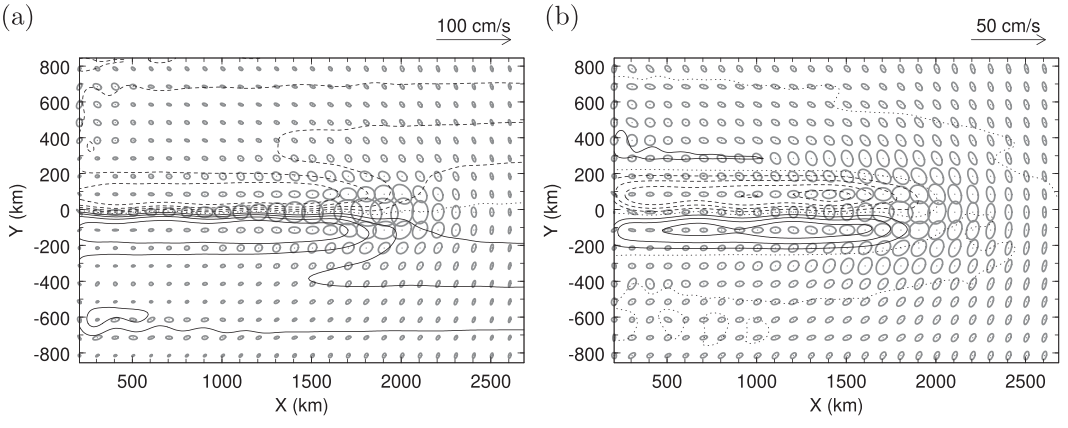


FIG. 1. The mean flow and the velocity perturbation in the (a) surface layer and (b) deep layer. Contours indicate the mean geostrophic streamfunction. The major and minor axes of the ellipses indicate the principal axes of the velocity perturbation (Emery and Thomson 2001). Solid and dashed contours indicate positive and negative values, respectively. Contour intervals are 0.4 m^2 s^{-2}.

Brought to you by HOKKAIDO DAIGAKU | Unauthenticated | Downloaded 05/13/26 12:03 AM UTC

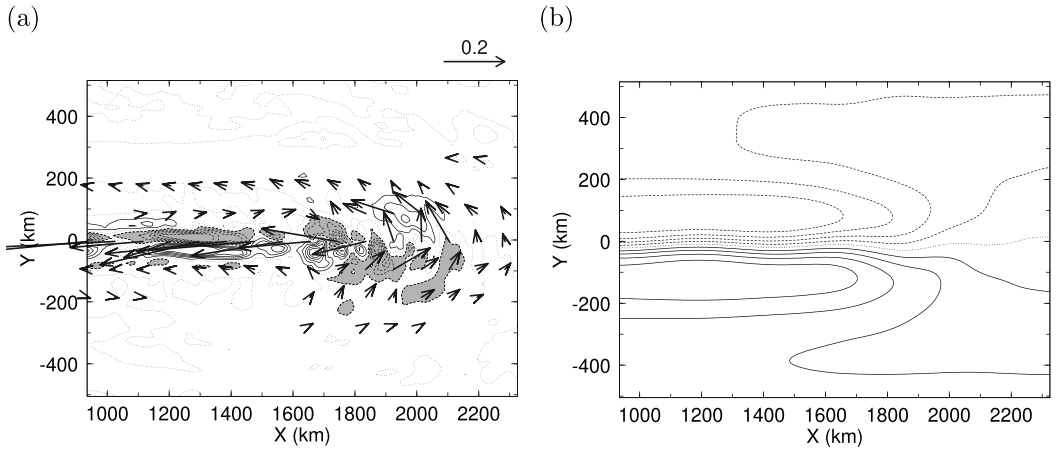


FIG. 2. (a) Vectors of the eddy PV flux and contours of the convergence of the eddy PV flux in the surface layer. (b) Contours of the mean geostrophic streamfunction in the surface layer. Contour intervals are 3×10^{-13} s^{-2} in (a) and 0.4 m^2 s^{-2} in (b). Shaded regions in (a) indicate negative values (i.e., divergence). Vectors are scaled by 1×10^{-6} m s^{-2}.

tend to be dominated by a rotational (i.e., divergence free) component that does not affect the mean flow (Lau and Wallace 1979). Eddy-resolving models depict the eddy heat flux as tending to be locally southward (i.e., upgradient) in the Gulf Stream and the Kuroshio Extension owing to this rotational component, even though the zonally integrated eddy heat flux is northward (Jayne and Marotzke 2002; Aoki et al. 2013).

In the experiment conducted by Haidvogel and Rhines (1983), the EE of the Rossby wave is produced by oscillatory forcing, while the mean flow advecting the EE is weak relative to the perturbation. This forcing is not explicitly included in (1), but the equation of the perturbation PV is expressed as

$$\frac{\partial q'}{\partial t} = -\bar{\mathbf{u}} \cdot \nabla q' - \mathbf{u}' \cdot \nabla \bar{q} - \nabla \cdot (\mathbf{u}' q')' + D', \qquad (2)$$

where t is the time and $(\mathbf{u}'q')' = \mathbf{u}'q' - \overline{\mathbf{u}'q'}$; thus, the oscillatory forcing w in Haidvogel and Rhines (1983) can be regarded as a parameterization of the third term on the right-hand side of (2), which represents the nonlinear interaction of different eddies, i.e., $w = -\nabla \cdot (\mathbf{u}'q')'$. This term is referred to as the eddy forcing in this study. Multiplying (2) by q', averaging in time, and assuming the stationary state, we obtain (1). Thus, in contrast to the argument by Holland and Rhines (1980), the PUF tends to be balanced by the second term on the right-hand side of (1) when the Rossby wave is excited by the eddy forcing in an eastward jet. This term is referred to as the eddy–eddy interaction in this study. In the region where the eddy (or any other) forcing excites the Rossby wave, the wave activity density, which is proportional to the EE, is radiated out of the region by the Rossby wave (Vallis 2006). Thus, the eddy–eddy interaction tends to be positive to supply the EE of the Rossby wave. This implies that the PUF becomes positive from (1), and the eddy PV flux is oriented in the upgradient direction of the mean PV in such region. In the Gulf Stream and the Kuroshio Extension, perturbations may not be so weak relative to the mean flow as Holland and Rhines (1980) assumed. By using an eddy-resolving isopycnic primitive equation model, Wilson and Williams (2004) demonstrated that the eddy–eddy interaction is sufficiently large in the jet produced in the wind-driven double gyres, and thus the PUF is partly balanced by this term. Thus, the eddy forcing is a possible mechanism of the Rossby wave forcing and the upgradient PV flux.

c. *Purpose of this study*

Therefore, the mechanism maintaining the budget of EE, and thus recirculation gyres, is not yet fully understood. The purpose of the current study is to examine this mechanism, focusing on the surface layer. In particular, we examine whether eddy forcing contributes to the generation of the upgradient PV flux and the Rossby wave, as assumed by Haidvogel and Rhines (1983). Eddy motions in an eastward jet are complex, as they include different components such as the instability and Rossby waves. While the instability wave tends to dominate in the frequency band that has a period of a few tens of days, the Rossby wave tends to dominate in lower frequency bands (Mizuta 2009). Thus, we examine the budget of EE, dividing the perturbation into contributions from different frequency bands. We expect that the component relevant to the radiation of the Rossby wave can be extracted in such an analysis. The rest of this paper is organized as follows: The numerical experiment is described in section 2, the results of the numerical experiment are analyzed in section 3, additional experiments are performed in section 4 to further understand the results from the previous section, and the overall results are summarized in section 5.

2. Model

To reproduce the jet and recirculation gyres in an idealized setting, we conducted a numerical experiment using the Regional Ocean Modeling System (ROMS; Haidvogel et al. 2000), which is a free-surface, terrain-following, primitive equation model. Experimental conditions were basically the same as those used in Mizuta (2009), with an eastward jet being driven by the inflow and outflow prescribed at the

Brought to you by HOKKAIDO DAIGAKU | Unauthenticated | Downloaded 05/13/26 12:03 AM UTC

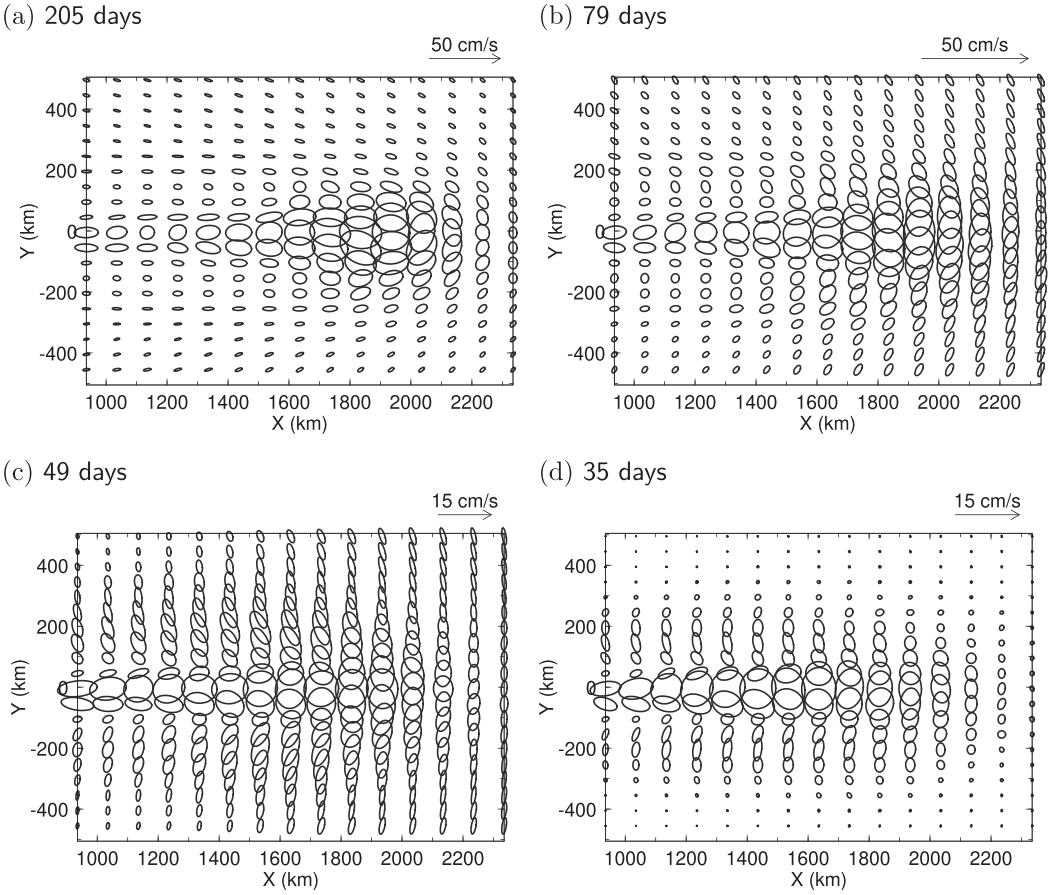


FIG. 3. The velocity perturbation in the (a) 205-, (b) 79-, (c) 49-, and (d) 35-day bands. The major and minor axes of the ellipses indicate the principal axes of the velocity perturbation in each frequency band.

western and eastern boundaries, respectively. In the real ocean, the eastward jet is formed when narrow western boundary currents separate from the coast, and this jet eventually broadens to join the interior Sverdrup flow. To represent these features, the inflow was proportional to $1/\cosh^2(y/L_{\text{in}})$, and the outflow was uniform in the y direction, where x, y, and z denote the eastward, northward, and upward coordinates, respectively, and $(x, y, z) = (0, 0, 0)$ corresponds to the surface at the central latitude of the western boundary (see the appendix for details). The model domain was a rectangle placed on the β plane with a flat bottom.

Both the inflow and outflow exponentially decayed from the surface with the e-folding scale of 750 m, except that the vertical shear decreased near the surface. The vertical structure of the inflow and outflow and the stratification were determined based on the values near the Kuroshio Extension given in the *World Ocean Atlas 2005* (Locarnini et al. 2006; Antonov et al. 2006; see the appendix for details). The horizontal scale L_{in} of the inflow was 30 km, and the maximum speed u_0 of the inflow at the surface was 0.8 m s^{-1}, resulting in the transport of 39×10^6 m^3 s^{-1}. The Coriolis parameter f_0 at $y = 0$ was 9×10^{-5} s^{-1}; the meridional gradient β of the Coriolis parameter was 2×10^{-11} m^{-1} s^{-1}; the bottom depth H_0 was 4000 m; and the zonal and meridional dimensions of the model domain were 5120 and 1920 km, respectively. The first internal deformation radius based on the stratification and the Coriolis parameter was 30 km at $y = 0$. To suppress the reflection of perturbations, a sponge layer was imposed near all four boundaries. The linear damping coefficient of velocity and density within this layer increased from zero to $\gamma_s = 1/20$ day^{-1} toward the boundary. Other conditions for the numerical experiment are listed in Table 1. After a spinup of over 4000 days, in which the eddy kinetic energy nearly reached a constant, the model equation was integrated over another 8000 days. We analyzed model results averaged every 4 days between 4000 and 12 000 days. Basic features of the results did not change even if the inflow speed or the horizontal distribution of the outflow was altered.

Because the flow is nearly adiabatic, we analyzed variables interpolated onto four isopycnal surfaces, which are located at depths of ~400, 1020, 2150, and 3300 m. The first and last isopycnal surfaces are referred to as the surface and deep layers, respectively. We interpolated the eastward velocity u and the northward velocity v and the pressure p into these isopycnal surfaces, and we then calculated the geostrophic streamfunction,

Brought to you by HOKKAIDO DAIGAKU | Unauthenticated | Downloaded 05/13/26 12:03 AM UTC

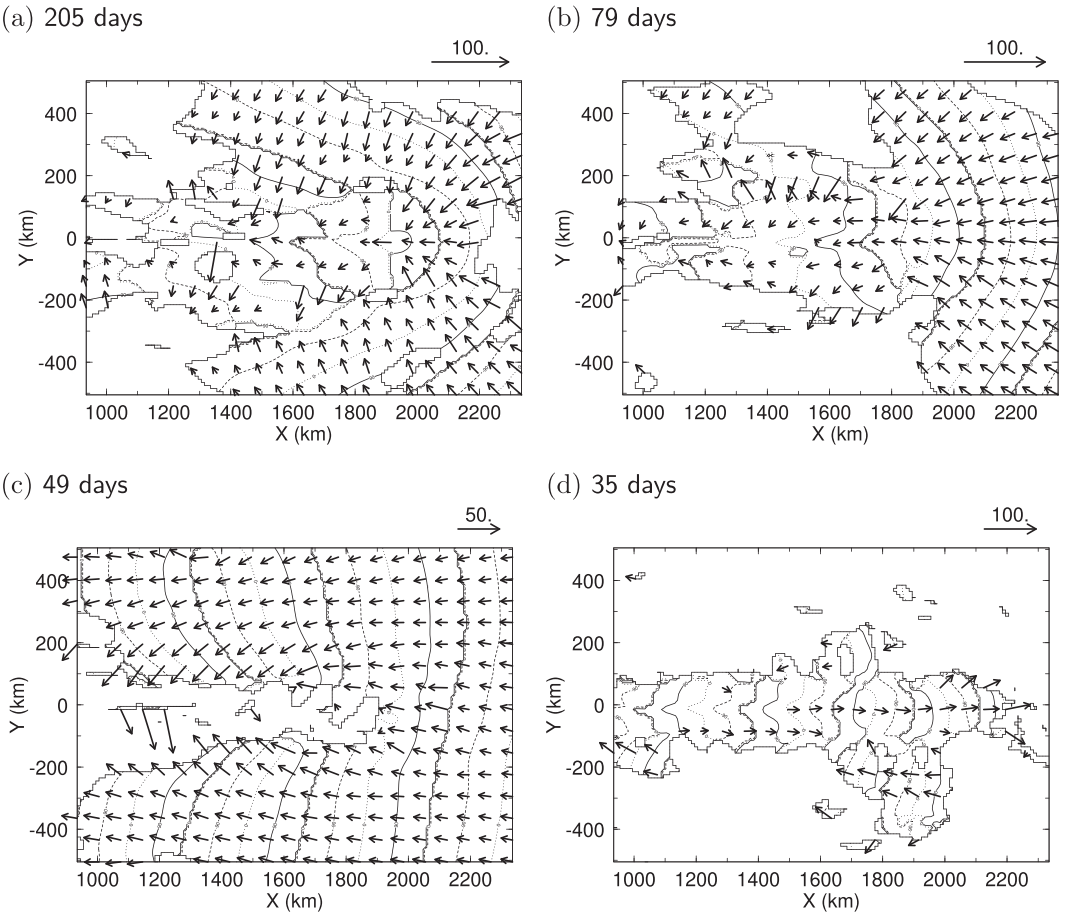


FIG. 4. Contours of the phase of the velocity component parallel to the major principal axis in the (a) 205-, (b) 79-, (c) 49-, and (d) 35-day bands in the surface layer. Contour intervals are 90°. Vectors indicate the gradient of the phase, which represents the propagation direction of the phase. Contours are not drawn for the region in which the 95% confidence interval exceeds 30°. Vectors are scaled by 1×10^{-6} m^{-1}.

$$\pi = \frac{p + g\rho z}{\rho_b}, \tag{3}$$

and the quasigeostrophic PV,

$$q = \zeta - \frac{f_0 h}{H} + \beta y. \tag{4}$$

Here, ρ is the density, z is the depth of the isopycnal surface, g is the gravity acceleration, ρ_b is the Boussinesq density, $\zeta = v_x - u_y$ is the relative vorticity, and H and h are the average and perturbation from the average of the thickness between two isopycnals, respectively (Vallis 2006). The ratios $|\zeta|/f_0$ and $|h|/H$, which represent the accuracy of the quasigeostrophic approximation, were less than about 0.1.

Next, we calculated the autospectra and cross-spectra between q' and (u', v'), dividing the time series of q' and (u', v') into 30 overlapping segments of 512 days and tapering each segment by a Hanning window. We averaged these spectra over all segments and four adjacent frequencies. The mean frequencies of the lowest four frequency bands were 0.005, 0.013, 0.021, and 0.028 cycles per day (cpd), which correspond to the periods of 205, 79, 49, and 35 days, respectively. These frequency bands are referred to as the 205-, 79-, 49-, and 35-day bands, respectively. From Parseval's theorem,

$$\int_{-\infty}^{+\infty} \phi_1(t)\phi_2(t)dt = \frac{1}{2\pi}\int_{-\infty}^{+\infty} \tilde{\phi}_1(\omega)\tilde{\phi}_2^*(\omega)d\omega, \tag{5}$$

where $\phi_1(t)$ and $\phi_2(t)$ are arbitrary real functions of time, ω is the angular frequency, and the tilde and the asterisk denote the Fourier component and the complex conjugate, respectively. The integral of the autospectra of q' coincides with $\overline{q'^2}$ [which is confirmed by substituting $\phi_1 = \phi_2 = q'$ to (5)]. Thus, half the autospectra of q' represent the EE decomposed into different frequency bands. Similarly, the cross-spectra between q' and (u', v') represent the eddy PV flux decomposed into different frequency bands [which is confirmed by substituting $\phi_1 = q'$, $\phi_2 = u'$ or v' to (5)].

We also extracted the most dominant pattern of perturbations in each frequency band using the technique of the

Brought to you by HOKKAIDO DAIGAKU | Unauthenticated | Downloaded 05/13/26 12:03 AM UTC

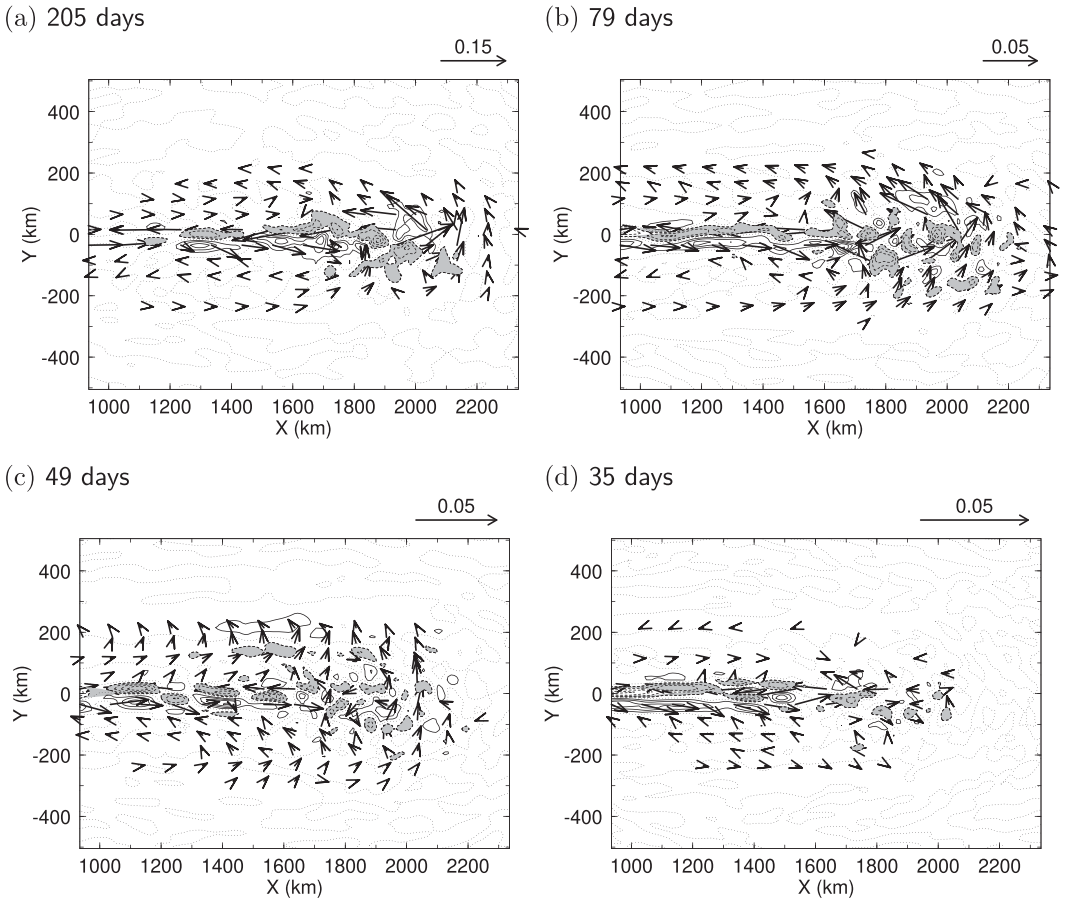


FIG. 5. Vectors of the PV flux and contours of the convergence of the eddy PV flux in the (a) 205-, (b) 79-, (c) 49-, and (d) 35-day bands in the surface layer. Contour intervals are 3×10^{-13}, 1.5×10^{-13}, 1×10^{-13}, and 0.8×10^{-13} s^{-2} in (a)–(d), respectively. Vectors are scaled by 1×10^{-6} m s^{-2}.

empirical orthogonal functions in the frequency domain (FDEOFs; Wallace and Dickinson 1972), as in Mizuta (2009). In contrast to the conventional empirical orthogonal functions, FDEOFs are complex and represent the distribution of both the amplitude and the phase of dominant perturbations. We calculated the FDEOFs by combining u, v, and z on the four representative isopycnals defined above to extract perturbations extending over the entire water column. These variables were weighted so that the variance of weighted (u, v) and z was proportional to the kinetic and potential energy, respectively.

3. Results

a. *Eddy PV flux*

First, we examine properties of the mean flow and perturbation that were not decomposed into different frequency bands. Figure 1 shows the jet and perturbation in the surface and deep layers, with the mean geostrophic streamfunction $\overline{\pi}$ and the principal axes of the velocity perturbation. The sponge layers and the eastern region are omitted. In the surface layer, the eastward jet extends from $x = 0$ to 1800 km (Fig. 1a). Two recirculation gyres are produced on the southern and northern flanks of the jet in both the surface and deep layers (Figs. 1a,b). The eastward jet broadens at the eastern end of the recirculation gyres (Fig. 1a). Part of the outflow imposed at the eastern boundary directly reaches the western boundary in $y > 600$ km and < -600 km. This corresponds to the linear solution of the circulation driven by the outflow. The recirculation gyres and the linear solution coexist also in the double gyre circulation (Haidvogel et al. 1992; Nakano et al. 2008). The transport of each recirculation gyre, which is integrated from the surface to the bottom, was $\sim 30 \times 10^6$ m^3 s^{-1}, though it depends on the definition of the boundary of the gyres. The total downstream transport and throughflow transport, which include and do not include the transport of recirculation gyres, respectively, of the Kuroshio and Kuroshio Extension were estimated by several observational studies. Imawaki et al. (2025) estimate the mean throughflow transport of 35×10^6 m^3 s^{-1} at about 133°E. Jayne et al. (2009) estimate the total downstream transport of 114×10^6 and 79×10^6 m^3 s^{-1} in the stream and geographic coordinates at about 146°E, respectively. These transports roughly coincide with those in our experiment.

The velocity perturbation attains a maximum near the eastern end of the jet in both the surface and deep layers (Fig. 1).

Brought to you by HOKKAIDO DAIGAKU | Unauthenticated | Downloaded 05/13/26 12:03 AM UTC

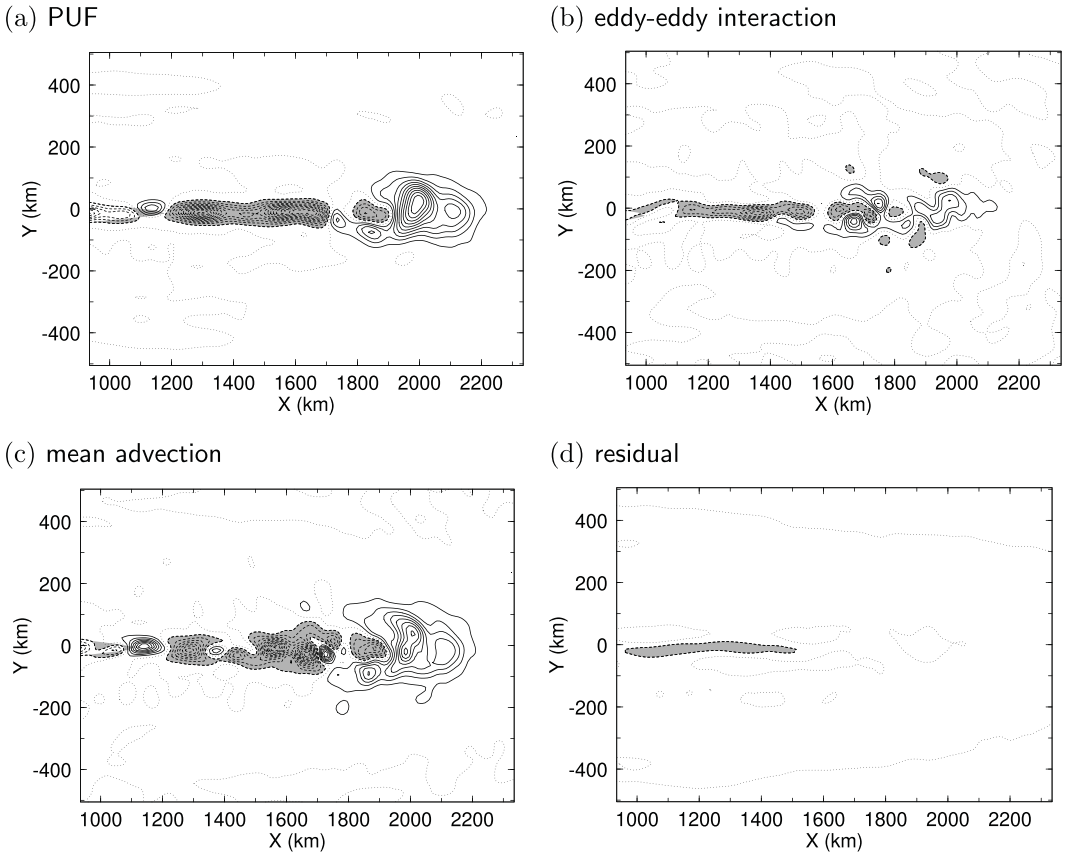


FIG. 6. Terms in the equation of the EE [(7)] for the low-frequency bands in the surface layer. Contours of the (a) production of the EE by the upgradient/downgradient PUF, (b) eddy–eddy interaction, (c) mean advection, and (d) residual. Contour intervals are 1×10^{-18} s^{-3}.

Note that the scale of the velocity perturbation differs between Figs. 1a and 1b. The perturbation in the surface layer is stronger than that in the deep layer. The major principal axis of the velocity perturbation is oriented in the northwest–southeast and northeast–southwest directions in a broad area on the northern and southern sides of the jet, respectively. The direction of motions, indicated by the major principal axis, is consistent with that produced by the Rossby wave in the experiment of Haidvogel and Rhines (1983), indicating that the Rossby wave is radiated from the eastern end of the jet (Mizuta 2009; Waterman and Jayne 2011). While a large velocity perturbation is concentrated near the jet in the surface layer, such a perturbation extends over a broader area in the deep layer (Figs. 1a,b). The perturbation in the jet is weaker in the deep layer than that in the surface layer. In the following analysis, we focus on the surface layer, where the perturbation is strong.

Figure 2 shows the eddy PV flux in the surface layer in the area near the recirculation gyres. The eddy PV flux is northward, that is, in the upgradient direction of the mean PV, near the eastern end of the recirculation gyres ($x = 2000$ km). Converging and diverging in the northern and southern regions, respectively, the upgradient PV flux tends to drive the recirculation gyres to satisfy the equation of the mean PV:

$$\overline{\mathbf{u}} \cdot \nabla \overline{q} = -\nabla \cdot \overline{\mathbf{u}' q'} + \overline{D}. \tag{6}$$

In the relatively upstream region ($x < 1600$ km), the PV flux diverges and converges on the northern and southern flanks of the jet, respectively, corresponding to the southward (i.e., downgradient) PV flux. (Although the PV flux is mainly zonal in the upstream region, it also includes the downgradient component at $y = 0$ km.) These divergence and convergence of the PV flux tend to broaden the jet.

Next, we decompose the perturbation and eddy PV flux in the surface layer into different frequency bands. To examine the propagation direction of the perturbation, we also calculate the FDEOFs. To save computation time, we calculated the FDEOFs from u, v, and z for $1850 < x < 2100$ km and $-350 < y < 350$ km and obtained the regression of each variable to the FDEOFs in the entire model domain. The first FDEOF explains 32%, 30%, 39%, and 32% of the total energy in the 205-, 79-, 49-, and 35-day bands, respectively. The basic features of the FDEOFs were not affected by the details of the calculation method used to obtain them.

Figures 3a–d show the distribution of the velocity perturbation in the 205-, 79-, 49-, and 35-day bands, respectively. While the velocity perturbation is concentrated near the jet

Brought to you by HOKKAIDO DAIGAKU | Unauthenticated | Downloaded 05/13/26 12:03 AM UTC

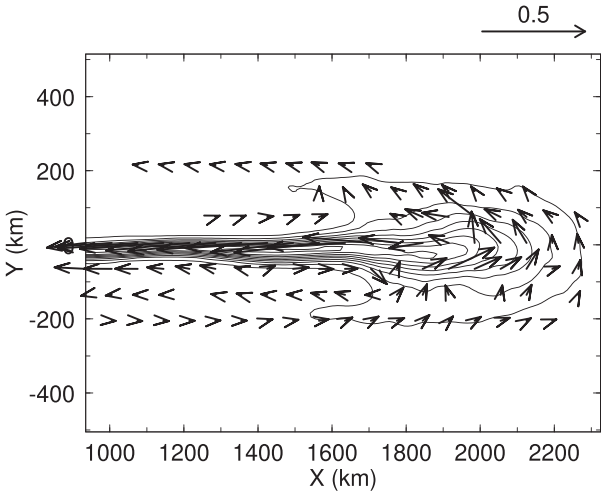


FIG. 7. Vectors of the eddy PV flux and contours of the EE in the surface layer. Contour intervals are 8×10^{-10} s^{-2}. Vectors are scaled by 1×10^{-6} m s^{-2}.

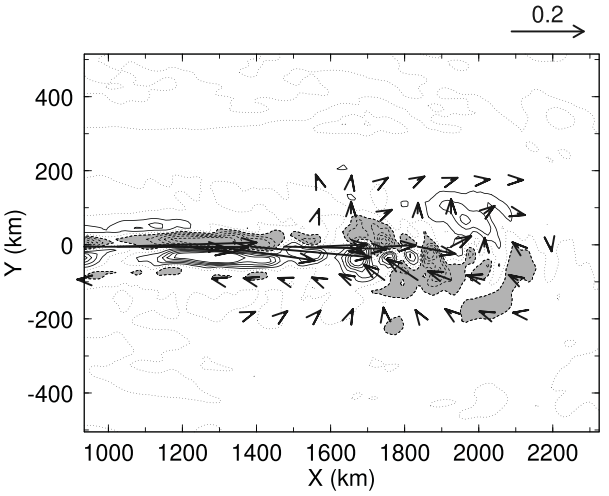


FIG. 9. Vectors of the eddy PV flux without the rotational component and contours of the convergence of the eddy PV flux in the surface layer. Contour intervals are 3×10^{-13} s^{-2}. Vectors are scaled by 1×10^{-6} m s^{-2}.

axis in the 35-day band, a large velocity perturbation extends over a broader area in the 205-, 79-, and 49-day bands. In these frequency bands, the major principal axis of the velocity perturbation is oriented in the northwest–southeast and northeast–southwest directions on the northern and southern sides of the jet, respectively, as in Fig. 1. The perturbation is strong in the upstream region of the jet ($x < 1700$ km) in the 35-day band; in the 205- and 79-day bands, it attains a maximum near the eastern end of the recirculation gyres ($x \sim 1800$ km). In contrast to the perturbations in the low-frequency bands, the major principal axis of the velocity perturbation in the 35-day band tends to be oriented in the northeast–southwest and northwest–southeast directions on the northern and southern sides of the jet near the jet axis in the upstream region ($x < 1400$ km), respectively (Fig. 3d). Thus, the divergence of the Reynolds stress, $(\overline{u'v'})_y$, in the meridional direction tends to decelerate the jet, indicating that barotropic instability dominates in the 35-day band.

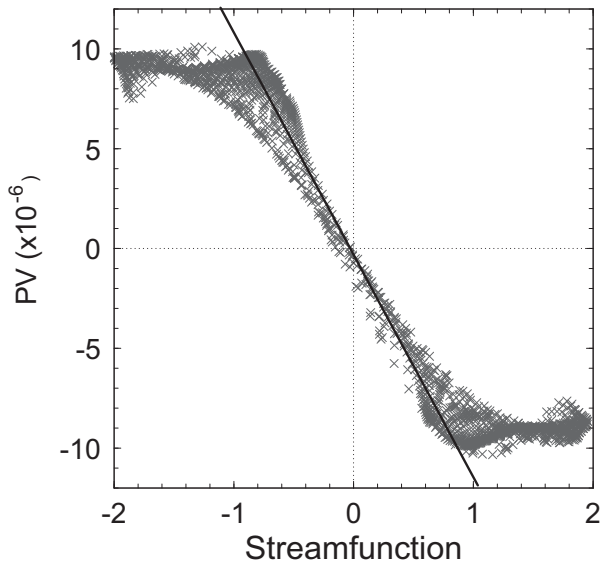


FIG. 8. Plot of the mean PV, $\overline{q}$ (s^{-1}), as a function of the mean geostrophic streamfunction, $\overline{\pi}$ (m^2 s^{-2}). The solid line indicates the line, $\overline{q} = A^{-1}\overline{\pi}$, obtained by linear fitting over $-0.6\,\mathrm{m^2\,s^{-2}} < \overline{\pi} < 0.6\,\mathrm{m^2\,s^{-2}}$.

Figure 4 shows the phase of the velocity component parallel to the major principal axis. The propagation direction of the perturbation is different between low- and high-frequency bands. In the 205-, 79-, and 49-day bands, the phase of the first FDEOF propagates southwestward and northwestward on the northern and southern sides of the jet, respectively (Figs. 4a–c). The propagation speed and vertical structure of the perturbation are consistent with those of a barotropic Rossby wave (Mizuta 2009). A baroclinic Rossby wave cannot propagate in these frequency bands because the frequency exceeds the critical value of the first baroclinic Rossby wave, $f_c = \pi\beta a_1 = 0.0041$ cpd, where a_1 is the first baroclinic deformation radius. Thus, from the dispersion relation of the barotropic Rossby wave, the energy of the Rossby wave propagates northward and southward from the jet, indicating that the jet is the source of the Rossby wave energy. In the 35-day band, in contrast, the phase of the first FDEOF propagates eastward (Fig. 4d).

Figure 5 shows the PV flux in each frequency band. At the eastern end of the recirculation gyres, the upgradient (northward) PV flux is generated in the 205- and 79-day bands, which are dominated by the Rossby wave. This finding is consistent with the experimental result obtained by Haidvogel and Rhines (1983). As was the case for the total field (Fig. 2), the upgradient PV flux in the 205-day band converges and diverges in the northern and southern regions, respectively (Fig. 5a). The PV flux in the 79-day band also tends to enhance these convergence and divergence of the PV flux (Fig. 5b). The perturbation in the 49-day band contributes to the upgradient PV

Brought to you by HOKKAIDO DAIGAKU | Unauthenticated | Downloaded 05/13/26 12:03 AM UTC

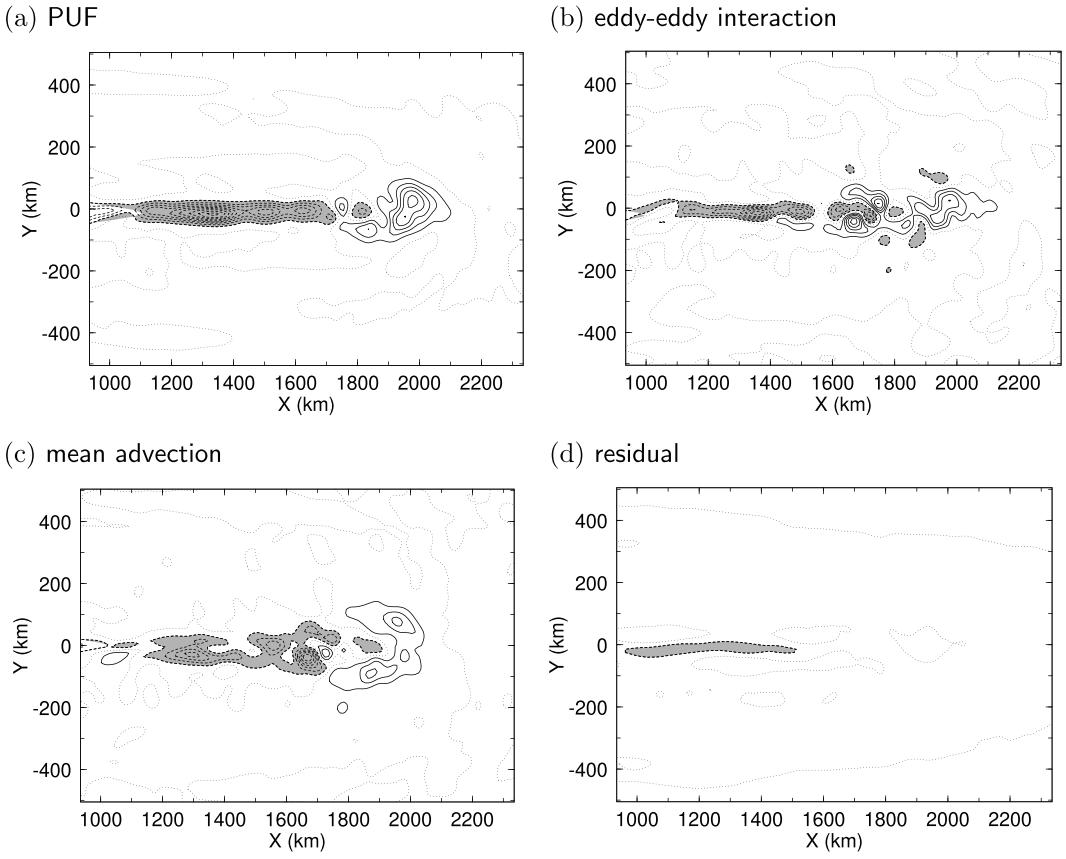


FIG. 10. Terms in the equation of the EE [(7)] without the rotational component for the low-frequency bands in the surface layer. Contours of the (a) PUF, (b) eddy–eddy interaction, (c) mean advection, and (d) residual. Contour intervals are 1×10^{-18} s^{-3}.

flux, but the convergence and divergence of the PV flux are not so clear (Fig. 5c). The perturbation in the 35-day band contributes to the convergence and divergence of the PV flux near the jet axis in the upstream region of the jet, which corresponds to the downgradient PV flux (Fig. 5d). Although figures are not shown, this downgradient PV flux is dominated by the relative vorticity flux and mostly corresponds to the divergence of the Reynolds stress shown in Fig. 3d owing to the relation, $\overline{v'\zeta'} \sim -(\overline{u'v'})_y$. The distribution of the perturbation and convergence of the PV flux in the 28- and 23-day bands are quite similar to those in the 35-day band (figures not shown). At frequencies higher than these bands, the convergence of the PV flux becomes small and less clear.

Thus, jet instability and Rossby wave radiation dominate in the upstream and downstream regions, respectively, as mentioned by Waterman and Jayne (2011). The low- and high-frequency perturbations are dominated by these Rossby and instability waves, respectively. In addition, the Rossby wave contributes to the generation of the upgradient PV flux, whereas the instability wave contributes to the generation of the downgradient PV flux. The convergence and divergence concentrated near the jet axis can also be observed in the upstream region ($x < 1600$ km) in the low-frequency bands, probably because the perturbation due to the instability wave is partly included.

Based on these features of the PV flux, we refer to the 205- and 79-day bands as the low-frequency bands, whereas we refer to the 35-, 28-, and 23-day bands as the high-frequency bands in the following analysis. The mean frequency of the low-frequency and high-frequency bands was 0.009 and 0.036 cpd, which correspond to the periods of 114 and 28 days, respectively.

b. *Enstrophy budget*

Taking the Fourier transform of (2) in time, multiplying by $\tilde{q}'^*$, and assuming the stationary state, we obtain the equation of the EE in each frequency band:

$$\tilde{\mathbf{u}}'\tilde{q}'^* \cdot \nabla\overline{q} = -\overline{\mathbf{u}} \cdot \nabla\frac{|\tilde{q}'|^2}{2} - \tilde{q}'^*\nabla \cdot (\widetilde{\mathbf{u}'q'}) + \tilde{D}'\tilde{q}'^*. \qquad (7)$$

Equation (7) corresponds to (1) decomposed into different frequency bands. As in (1), the first and second terms on the right-hand side of (7) represent the advection of the EE by the mean flow and the eddy–eddy interaction, respectively. The left-hand side represents the PUF. Because the Fourier

Brought to you by HOKKAIDO DAIGAKU | Unauthenticated | Downloaded 05/13/26 12:03 AM UTC

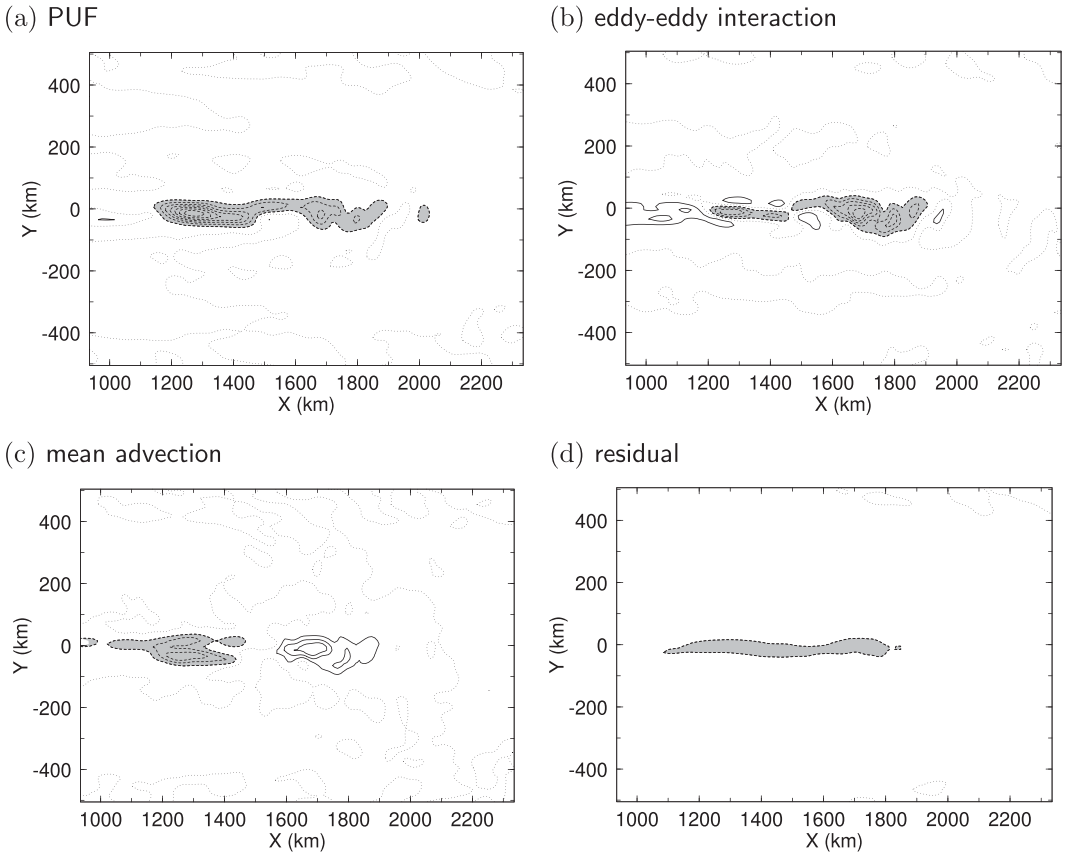


FIG. 11. Terms in the equation of the EE [(7)] without the rotational component for the high-frequency bands in the surface layer. Contours of the (a) PUF, (b) eddy–eddy interaction, (c) mean advection, and (d) residual. Contour intervals are 0.6×10^{-18} s^{-3}.

component of $\mathbf{u}'q'$ at the angular frequency of ω is expressed as

$$\widetilde{\mathbf{u}'q'} = \int_{-\infty}^{\infty} \tilde{\mathbf{u}}'(\omega')\tilde{q}'(\omega - \omega')d\omega', \tag{8}$$

the eddy–eddy interaction represents the exchange of EE between three different frequencies, ω, ω', and $\omega - \omega'$. We calculate these terms from the outputs of the numerical experiment, and the last term on the right-hand side of (7) is calculated as the residual of the other terms. In the following analysis, we refer to the first and third terms on the right-hand side of (7) as the mean advection and residual, respectively, whereas the second term on the right-hand side is the eddy–eddy interaction. From Parseval's theorem, the integral of the eddy–eddy interaction in (7) in frequency coincides with the corresponding term in (1). In general, this term does not vanish, while it vanishes when integrated horizontally over the entire model domain, because

$$-\overline{q'\nabla\cdot(\mathbf{u}'q')} = -\nabla\cdot\frac{\overline{\mathbf{u}'q'^2}}{2}, \tag{9}$$

identically.

Figure 6 compares each term in (7) integrated in the low-frequency bands, where the Rossby wave is dominant. Here, we applied a Gaussian filter with an e-folding scale of 20 km to smooth out small-scale features. The PUF is large near the eastern end of the recirculation gyres, $x = 2000$ km (Fig. 6a), which corresponds to the northward PV flux in Figs. 5a and 5b. The eddy–eddy interaction tends to have the same sign as the PUF in the same region (Fig. 6b). This suggests that the eddy forcing excites the Rossby wave because the PUF tends to be balanced by the production of the EE by the forcing of the Rossby wave as we considered in section 1b. However, the eddy–eddy

TABLE 2. Eddy–eddy interaction integrated in the region -100 km $< y <$ 100 and 1600 km $< x$. The first and second rows represent the eddy–eddy interaction in the low-frequency and high-frequency bands, respectively. The third row represents the sum of the eddy–eddy interaction in other frequency bands and residuals. The fourth row represents the convergence of the EE by eddy motions.

Low-frequency bands ($\times 10^{-8}$ m^2 s^{-3})	82
High-frequency bands ($\times 10^{-8}$ m^2 s^{-3})	−37
Other ($\times 10^{-8}$ m^2 s^{-3})	−6
Convergence ($\times 10^{-8}$ m^2 s^{-3})	39

Brought to you by HOKKAIDO DAIGAKU | Unauthenticated | Downloaded 05/13/26 12:03 AM UTC

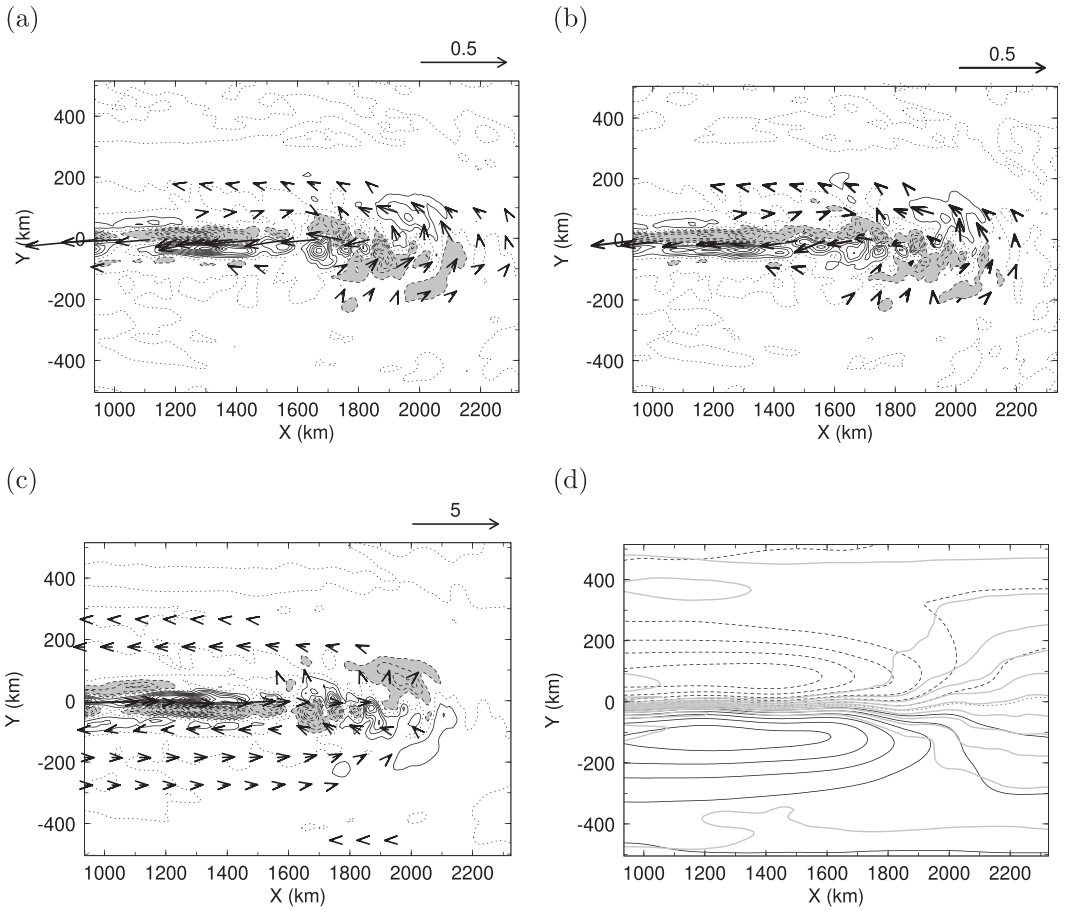


FIG. 12. Contours of the (a) convergence of the eddy PV flux; (b) convergence of the eddy PV flux integrated in the low-frequency, high-frequency, and 49-day bands; (c) convergence of the mean PV flux; and (d) mean geostrophic streamfunction in the surface layer. Vectors represent the eddy PV flux in (a) and (b) and the mean PV flux in (c). Gray contours in (d) represent the mean PV. Contour intervals are 3×10^{-13} s^{-2} in (a)–(c) and 0.3 m^2 s^{-2} and 2×10^{-6} s^{-1} for black and gray contours in (d), respectively. Vectors are scaled by 1×10^{-6} m s^{-2}.

interaction is smaller than the mean advection (Fig. 6c). The PUF is almost balanced by the mean advection.

Lau and Wallace (1979) showed that the large cancellation between the PUF and the mean advection tends to occur owing to the rotational component of the eddy PV flux. Thus, Marshall and Shutts (1981) introduced the rotational eddy PV flux:

$$(\overline{\mathbf{u}'q'})_R = \frac{A}{2}\left(-\frac{\partial\overline{q'^2}}{\partial y}, \frac{\partial\overline{q'^2}}{\partial x}\right), \tag{10}$$

where A is a constant satisfying an empirical relation,

$$\overline{\psi} = A\overline{q}, \tag{11}$$

and $\overline{\psi} \sim \overline{\pi}/f_0$ is the mean streamfunction. Taking the dot product of (10) with $\nabla\overline{q}$ and substituting (11) yields

$$\begin{aligned}(\overline{\mathbf{u}'q'})_R \cdot \nabla\overline{q} &= -A(-\overline{q}_y, \overline{q}_x) \cdot \nabla\left(\frac{\overline{q'^2}}{2}\right) \\ &= -\overline{\mathbf{u}} \cdot \nabla\left(\frac{\overline{q'^2}}{2}\right),\end{aligned} \tag{12}$$

so the mean advection is balanced by the production of the EE by the upgradient component of $(\overline{\mathbf{u}'q'})_R$. Because $(\overline{\mathbf{u}'q'})_R$ is parallel to the contour of the EE and nondivergent from (10), it does not contribute to driving the mean flow [see (6)]. Figure 7 compares the distribution of the EE and eddy PV flux in the surface layer. The PV flux tends to be parallel to the contour of the EE, indicating that the eddy PV flux includes a rotational component.

Thus, we subtracted the rotational component,

$$(\tilde{\mathbf{u}}'\tilde{q}'^*)_R \cdot \nabla\overline{q} = -A(-\overline{q}_y, \overline{q}_x) \cdot \nabla\left(\frac{|\tilde{q}'^2|}{2}\right), \tag{13}$$

from the left-hand side and the first term on the right-hand side of (7). The other terms in (7) remain unchanged. To determine the constant A, which is defined in (11), we fitted $\overline{q}$ by $\overline{\pi}$ for $1000 < x < 2200$ km (the solid line in Fig. 8), where the up- and downgradient PV flux are large. For the fitting, we used $(\overline{\pi}, \overline{q})$ for $-0.6\,\mathrm{m^2\,s^{-2}} < \overline{\pi} < 0.6\,\mathrm{m^2\,s^{-2}}$ because in this region, the PUF is large. Figure 9 shows the eddy PV flux

Brought to you by HOKKAIDO DAIGAKU | Unauthenticated | Downloaded 05/13/26 12:03 AM UTC

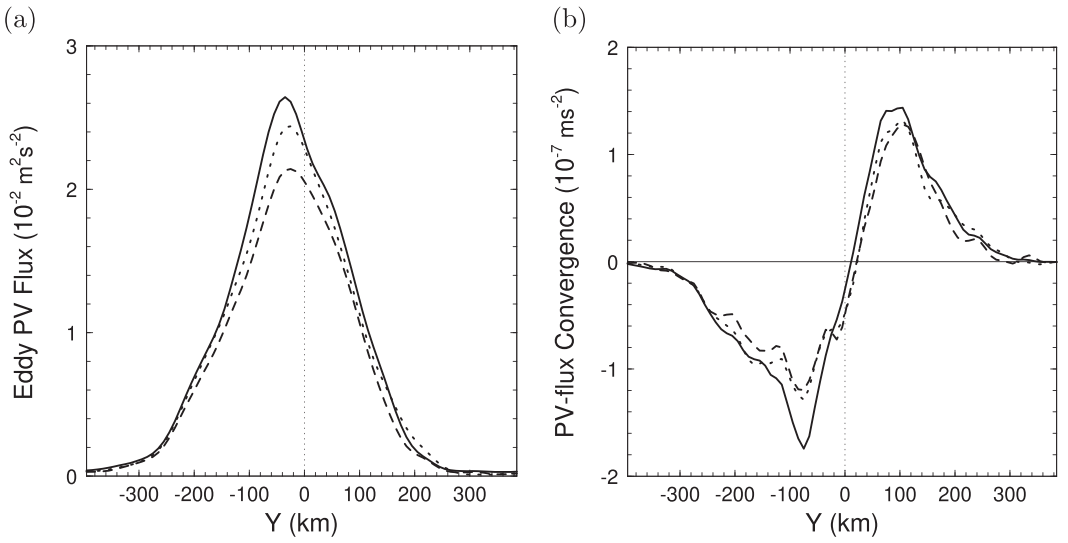


FIG. 13. Meridional distribution of the (a) northward eddy PV flux and (b) convergence of the eddy PV flux, which are integrated from $x = 1800$ to 2200 km in the surface layer. The solid, dashed, and dotted lines represent the PV flux and the convergence of it that were not decomposed into frequency bands, those integrated in the low-frequency bands, and those integrated in the low-frequency, high-frequency, and 49-day bands, respectively.

without the rotational component, which is not decomposed into different frequency bands. Compared with the eddy PV flux shown in Figs. 2 and 7, the eddy PV flux parallel to the contour of the EE is much reduced. In the above derivation, the condition (11) corresponds to a special case of the conservation of the mean PV along the mean streamfunction:

$$J(\overline{\psi}, \overline{q}) = 0, \tag{14}$$

where J is the Jacobian. It is implicitly assumed in (14) that the eddy PV flux does not affect $\overline{q}$. We return to this point in the next section.

Figure 10 shows each term in (7) without the rotational component integrated in the low-frequency bands. Now that the mean advection is weakened after subtracting $(\overline{\mathbf{u}'q'})_R$, the amplitude of the eddy–eddy interaction is similar to that of the PUF (Figs. 10a,b). The PV flux is oriented in the upgradient direction near the eastern end of the recirculation gyres (Fig. 10a). The PUF owing to this PV flux tends to be balanced by the eddy–eddy interaction (Figs. 10a,b). Thus, the Rossby wave excited by eddy forcing contributes to the generation of the upgradient PV flux, which directly drives the mean flow. The mean advection also partly balances the PUF. The residual tends to be large near the jet axis, indicating the dissipation of the strong perturbation in the jet.

Figure 11 shows each term of (7) without the rotational component integrated in the high-frequency bands in which the instability wave is dominant. The PV flux is oriented in the downgradient direction owing to the instability wave in the high-frequency bands (Fig. 11a). It is balanced by the mean advection in the upstream region, $x < 1600$ km, indicating that the EE produced by jet instability is advected downstream (Fig. 11c). In the downstream region, $x > 1600$ km, the increase in the EE by advection from the upstream region is balanced by the negative eddy–eddy interaction (Figs. 11b,c). The negative eddy–eddy interaction in Fig. 11b is also partly balanced by the negative PUF, which is shown in Fig. 11a, in the downstream region. This eddy–eddy interaction represents the transfer of the EE between different frequency bands [see (8)]. In almost the same region, the eddy–eddy interaction is positive in the low-frequency bands (Fig. 10b). Table 2 shows the eddy–eddy interaction in different frequency bands, which is integrated in the region -100 km $< y <$ 100 km and 1600 km $< x$. Nearly half of the eddy–eddy interaction in the low-frequency bands, which is shown in Fig. 10b, is balanced by that in the high-frequency bands, which is shown in Fig. 11b. Thus, the perturbation in the high-frequency bands contributes to generating the eddy forcing in the low-frequency bands. Then, as shown in Figs. 10b and 10c, this eddy forcing tends to excite the Rossby wave. As shown by (9), the sum of the eddy–eddy interaction in all frequency bands corresponds to the total flux of the EE, $\overline{\mathbf{u}'q'^2}/2$, by eddy motions converging into the region, which is shown at the bottom of Table 2. The precise mechanism of this convergence of the total EE flux is unknown.

c. *Eddy–mean flow interaction*

Figures 12a and 12b compare the sum of the eddy PV flux in the low-frequency, high-frequency, and 49-day bands with the original eddy PV flux. We can confirm that the eddy PV flux shown in Fig. 12a is nearly reproduced by the PV flux integrated in these three frequency bands. Figures 12c and 12d show the convergence of the mean PV flux and the mean streamfunction, respectively. The mean PV flux diverges and converges at the eastern end of the northern and southern recirculation gyres, where the mean geostrophic streamfunction (black contours in Fig. 12d) crosses the contour of the mean PV (gray contours) from south to north and from north to south, respectively

Brought to you by HOKKAIDO DAIGAKU | Unauthenticated | Downloaded 05/13/26 12:03 AM UTC

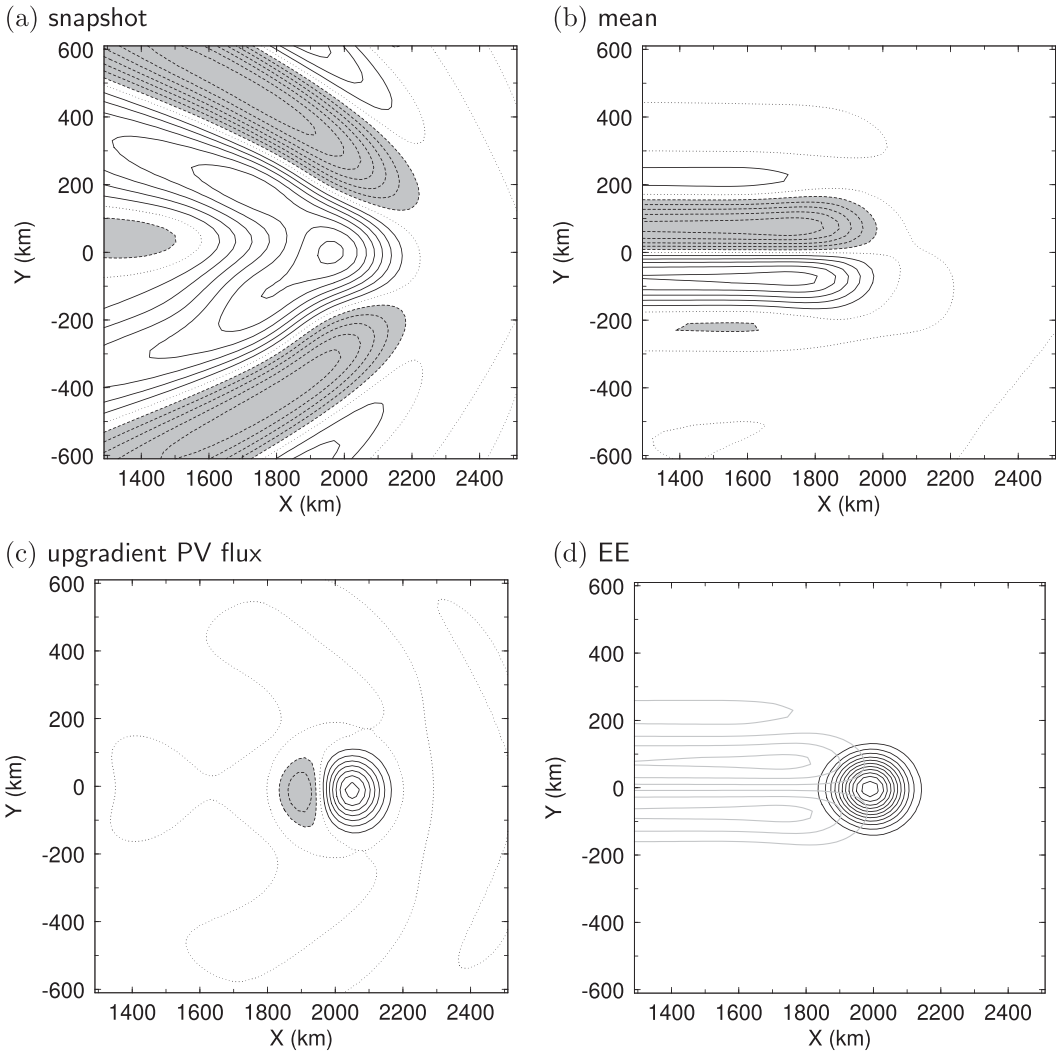


FIG. 14. Contours of the (a) snapshot geostrophic streamfunction at 4500 days, (b) mean geostrophic streamfunction, (c) upgradient PV flux, and (d) EE in the surface layer in the small-amplitude experiment. Contour intervals are 2×10^{-3} m^2 s^{-2}, 3×10^{-4} m^2 s^{-2}, 1.2×10^{-21} s^{-3}, and 5×10^{-15} s^{-2} in (a)–(d), respectively. Gray contours in (d) represent the mean geostrophic streamfunction.

[see (6)]. These convergence and divergence of the mean PV flux are nearly balanced by those of the eddy PV flux, indicating that the eddy PV flux drives the mean flow crossing the contour of the mean PV (Figs. 12a,c). Figure 13 shows the eddy PV flux integrated from $x = 1800$ to 2200 km in different frequency bands. We can confirm that the eddy PV flux in the low-frequency bands (dashed lines), which is dominated by the Rossby wave, mostly determines the eddy PV flux (solid lines) in these longitudes. Thus, the Rossby wave tends to drive the recirculation gyres.

In summary, the PV flux generated by the Rossby wave tends to drive the recirculation gyres. The eddy–eddy interaction contributes to exciting this Rossby wave in the low-frequency bands. The EE produced by jet instability in the upstream region in high-frequency bands is advected to the downstream region and transferred from the high- to low-frequency bands owing to the interaction between the high- and low-frequency perturbations. This eddy–eddy interaction tends to excite the Rossby wave. These processes of the Rossby and instability waves are consistent with Waterman and Jayne (2011).

The PV flux described above can be partitioned into the relative vorticity and potential thickness fluxes. Although the downgradient PV flux near the jet axis, which is shown in Fig. 2a, is dominated by the relative vorticity flux in the surface layer, the downgradient potential thickness flux, which tends to reduce the isopycnal slope of the jet, is dominant in the deep layer (figures not shown). Thus, the jet instability corresponds to mixed barotropic–baroclinic instability. In the downstream region, the potential thickness flux is oriented in the upgradient and downgradient directions of the mean PV in the surface and deep layers, respectively, whereas the relative vorticity flux is oriented in the upgradient direction in both

Brought to you by HOKKAIDO DAIGAKU | Unauthenticated | Downloaded 05/13/26 12:03 AM UTC

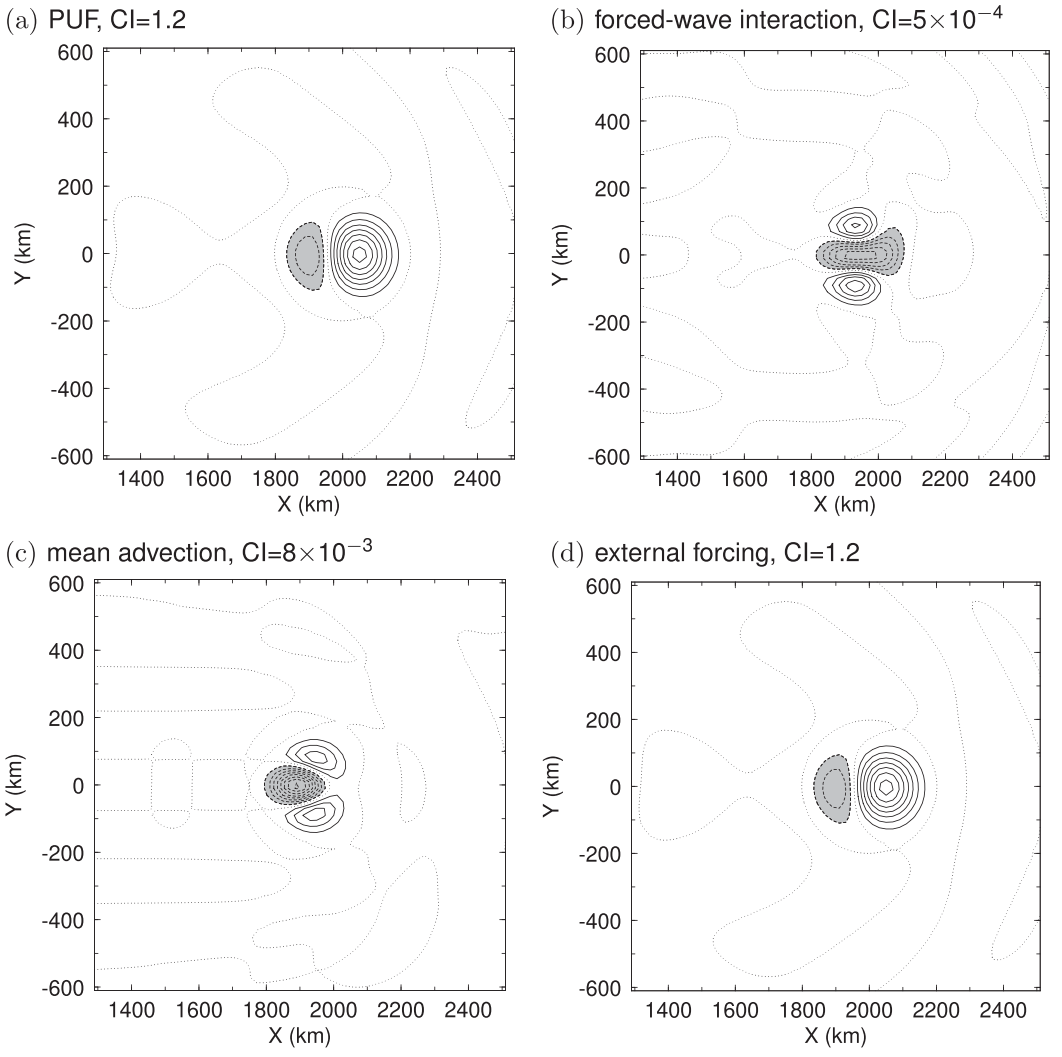


FIG. 15. Terms in the equation of the EE [(24)] for the small-amplitude experiment in the surface layer. Contours of the (a) PUF, (b) forced-wave interaction, (c) mean advection, and (d) external forcing. CIs, which are scaled by 1×10^{-21} s^{-3}, are shown in the title of each panel.

the surface and deep layers. Dominated by the potential thickness flux, the PV flux is oriented in the downgradient direction in the deep layer as shown by Holland and Rhines (1980).

4. Experiments with oscillatory forcing

In the previous section, we showed that the eddy–eddy interaction contributes to generating the upgradient PV flux. However, the amplitude of the mean advection is similar to that of the eddy–eddy interaction, even after subtracting the rotational component (Fig. 10). Therefore, we further examine the physical mechanism that maintains the mean advection in this section. In our experiment, the mean flow in the surface layer consists of two components: the eastward flow, which is directly driven by the inflow and outflow at the boundaries, and the recirculation gyres, which are driven by eddies. The assumption expressed by (11) or (14), which we used to obtain $(\overline{\mathbf{u}'q'})_R$, may be approximately satisfied in the former component. However, this is not the case for the latter component because the convergence of the eddy PV flux, $-\nabla \cdot \overline{\mathbf{u}'q'}$, which is neglected in (14), drives the recirculation gyres. Thus, we expect that $(\overline{\mathbf{u}'q'})_R$ dominates solely in the former component of the mean flow. This idea is supported by the numerical experiment because a large cancellation between the PUF and the mean advection does not occur in the deep layer, where the inflow and outflow are not applied (not shown). Thus, we examine the mean advection in an idealized experiment in which the Rossby wave is excited by oscillatory forcing instead of the eddy forcing in the jet, as in Haidvogel and Rhines (1983). The inflow and outflow at the boundary are not considered.

a. Formulation

Following Haidvogel and Rhines (1983), we represent the eddy forcing by an external forcing localized in space and

Brought to you by HOKKAIDO DAIGAKU | Unauthenticated | Downloaded 05/13/26 12:03 AM UTC

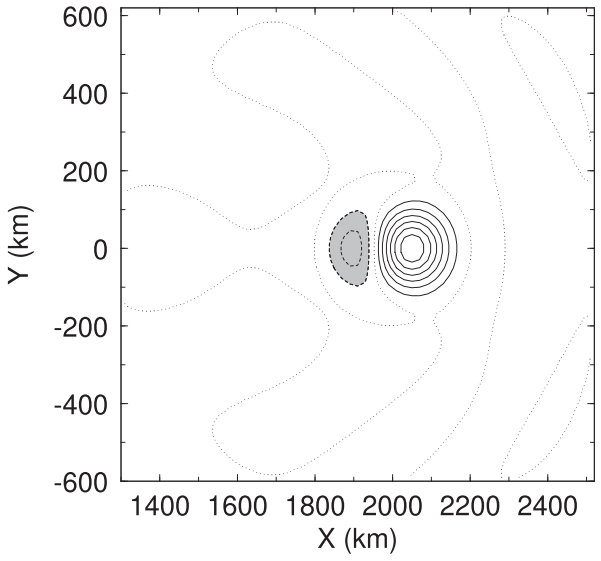


FIG. 16. Contours of the $O(1)$ PUF predicted by (25) in the surface layer. Contour intervals are $1.2 \times 10^{-21}\ \mathrm{s}^{-3}$.

oscillating in time. Scaled by the characteristic scales of horizontal length L, velocity U, and time T, and the bottom depth H_0, the nondimensional equation of the quasigeostrophic PV in a continuously stratified fluid becomes

$$\frac{\partial \hat{q}}{\partial \hat{t}} + \hat{\beta}\hat{v} = -\epsilon J(\hat{\psi}, \hat{Q}) + \hat{W}_E e^{-i\hat{\omega}\hat{t}}, \tag{15}$$

where a hat represents a scaled variable, $\hat{W}_E(x, y, z)$ represents the amplitude of the external forcing, $\hat{\omega}$ is the angular frequency of the forcing, and $\hat{q}$ is decomposed into $\hat{\beta}\hat{y}$ and $\hat{Q}$. The real part is implied in (15). The first and second terms on the right-hand side represent the eddy and external forcings, respectively. As we will see later, the former represents the eddy forcing owing to the Rossby wave excited by the external forcing. In the following analysis, we drop the hat for simplicity.

When the nondimensional parameter, $\epsilon = UT/L$, is small, we expand ψ and q in an asymptotic series in ϵ, that is,

$$\psi = \psi_0 + \epsilon\psi_1 + \epsilon^2\psi_2 + \cdots. \tag{16}$$

Substituting (16) into (15), we obtain the equation of the $O(1)$ PV,

$$-i\omega q_0^a + \beta v_0^a = W_E, \tag{17}$$

and the equation of the $O(\epsilon)$ PV,

$$\beta\overline{v}_1 = -\frac{1}{2}J(\psi_0^a, q_0^{a*}), \tag{18}$$

and

$$-2i\omega q_1^b + \beta v_1^b = -\frac{1}{2}J(\psi_0^a, q_0^a) \equiv W_1^b, \tag{19}$$

where the $O(1)$ and $O(\epsilon)$ variables are expressed as

$$\psi_0 = \psi_0^a e^{-i\omega t} \tag{20}$$

and

$$\psi_1 = \overline{\psi}_1 + \psi_1^b e^{-2i\omega t}, \tag{21}$$

respectively. The superscripts a, b, … represent components oscillating at the frequency of ω, 2ω, …. Equations (17)–(19) imply that the external forcing excites the $O(1)$ Rossby wave, and the eddy forcing by this $O(1)$ wave drives the mean flow and the $O(\epsilon)$ wave with twice the original frequency.

Higher-order waves are subsequently excited by the eddy forcing. The equation of the $O(\epsilon^2)$ PV is

$$-i\omega q_2^a + \beta v_2^a = -J(\psi_0^a, \overline{q}_1) - J(\overline{\psi}_1, q_0^a) - \frac{1}{2}[J(\psi_0^{a*}, q_1^b) + J(\psi_1^b, q_0^{a*})]$$
$$\equiv W_2^{aA} + W_2^{aB} + W_2^{aC}, \tag{22}$$

where the $O(\epsilon^2)$ variables are expressed as

$$\psi_2 = \psi_2^a e^{-i\omega t} + \psi_2^c e^{-3i\omega t}. \tag{23}$$

For convenience, we express the first, second, and the third terms on the right-hand side of (22) as W_2^{qA}, W_2^{qB}, and W_2^{qC}, respectively. An equation for q_2^c is not used and is thus omitted. We can solve Eqs. (17), (19), and (22) by using a Green's function (Mizuta 2018).

Decomposing the variables in (15) into the time average and the perturbation from the average and multiplying by q', we obtain the equation of the EE,

$$\beta\overline{v'q'} + \epsilon\overline{\mathbf{u}'q'} \cdot \nabla\overline{Q} = -\epsilon J\left(\overline{\psi}, \frac{\overline{q'^2}}{2}\right) - \epsilon\overline{q'J(\psi', q')} + \overline{q'\mathrm{Re}W_E e^{-i\omega t}}, \tag{24}$$

in the stationary state, where Re denotes the real part. The left-hand side in (24) represents the PUF. From (24), this PUF is primarily balanced by the third term on the right-hand side of (24), which represents the production of the EE by the external forcing. The second term on the right-hand side of (24) represents the eddy–eddy interaction between the Rossby waves. Because $W_E e^{-i\omega t}$ represents the eddy forcing, the eddy–eddy interaction in section 3 corresponds to the sum of the second and third terms on the right-hand side of (24). The first term on the right-hand side of (24) represents the mean advection. In the following analysis, the first, second, and third terms on the right-hand side of (24) are referred to as the mean advection, forced-wave interaction, and external forcing, respectively.

We can predict the $O(1)$ terms in (24) using the $O(1)$ equation of the EE,

$$\beta v_0^a q_0^{a*} = W_E q_0^{a*}, \tag{25}$$

which we obtain by multiplying (17) by q_0^{a*} and neglecting pure imaginary terms. The $O(1)$ component of the external forcing is given by the right-hand side of (25). Similarly, to predict the mean advection, we use the $O(\epsilon^2)$ equation of the EE, which is obtained from (17), (19), and (22) as

Brought to you by HOKKAIDO DAIGAKU | Unauthenticated | Downloaded 05/13/26 12:03 AM UTC

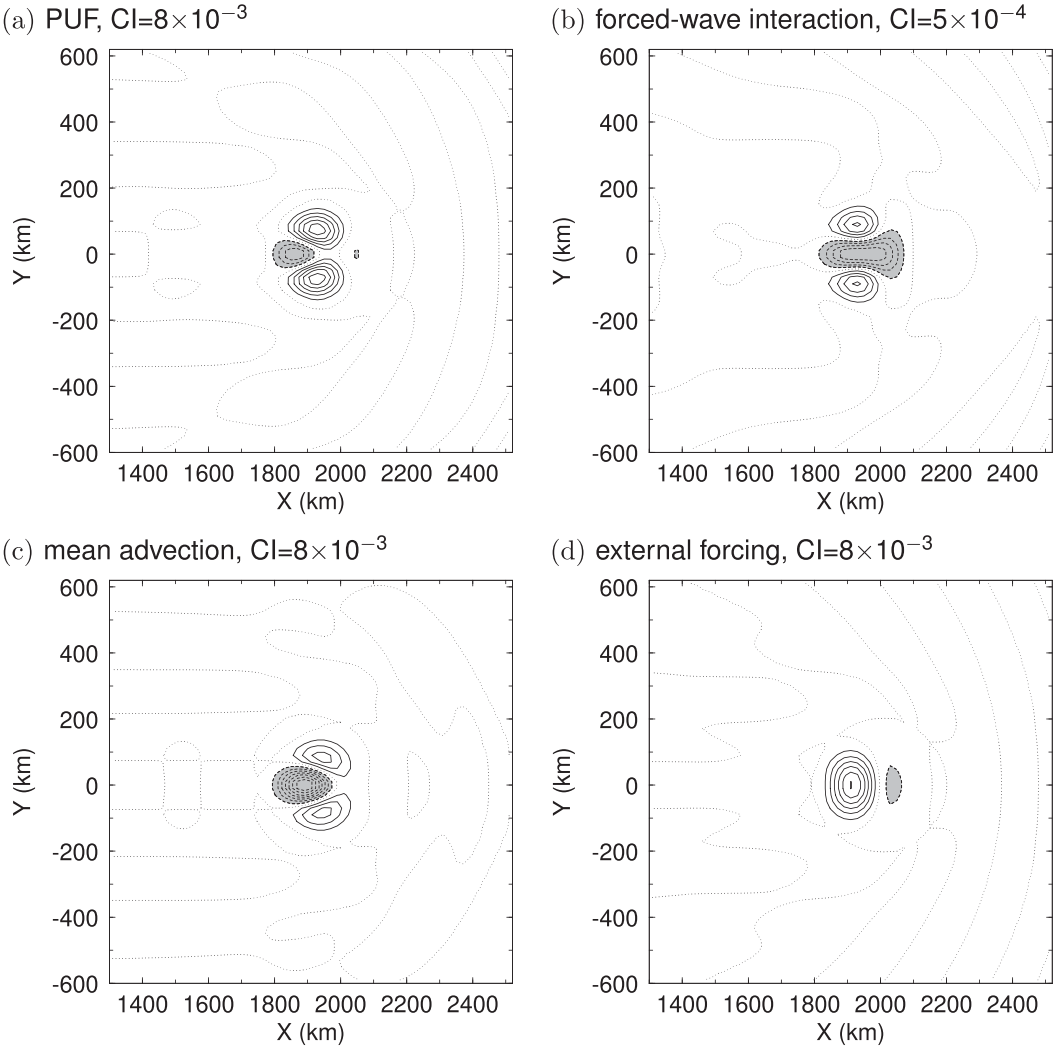


FIG. 17. The $O(\epsilon^2)$ terms in the equation of the EE predicted by (26) in the surface layer. Contours of the $O(\epsilon^2)$ (a) PUF, (b) forced-wave interaction, (c) mean advection, and (d) external forcing. CIs, which are scaled by 1×10^{-21} s^{-3}, are shown in the title of each panel.

$$\beta(v_0^a q_2^{a*} + v_2^a q_0^{a*} + v_1^b q_1^{b*}) + \boldsymbol{u}_0^a q_0^{a*} \cdot \nabla \overline{q}_1$$

$$= -J\left(\overline{\psi}_1, \frac{|q_0^a|^2}{2}\right) + (W_2^{aC} q_0^{a*} + W_1^b q_1^{b*}) + W_E q_2^{a*}. \quad (26)$$

Note that the $O(\epsilon)$ terms in the equation of the EE are absent. The lowest-order component of the mean advection is given by the first term on the right-hand side of (26). This term implies that the mean advection corresponds to the advection of the $O(1)$ EE by the mean flow, which is driven by the $O(1)$ Rossby wave [see (18)]. The second and third terms on the right-hand side of (26) represent the forced-wave interaction [see (22)] and the $O(\epsilon^2)$ external forcing [see (17)], respectively. The left-hand sides in (25) and (26) represent the $O(1)$ and $O(\epsilon^2)$ PUF, respectively. Thus, we can predict each term in (24) by using (25) and (26).

b. Numerical solution

Based on the formulation in the previous subsection, we performed numerical experiments using ROMS as in section 3. A body force,

$$\tau = (\tau_1' \cos\omega t, \tau_2' \cos\omega t)$$

$$= \left(-\frac{\partial \Psi_E}{\partial y} \cos\omega t, \frac{\partial \Psi_E}{\partial x} \cos\omega t\right), \quad (27)$$

was applied to the momentum equation, where Ψ_E was a Gaussian form in both the horizontal and vertical directions:

$$\Psi_E = \frac{A_f}{\sqrt{\pi}} \exp\left[-\frac{(x - x_c)^2 + y^2}{r_f^2}\right] \exp\left(-\frac{z^2}{h_f^2}\right). \quad (28)$$

Hence, W_E in (15) is expressed as $W_E = \tau_{2,x}' - \tau_{1,y}' = \nabla^2 \Psi_E$. The spatial scales of Ψ_E were $r_f = 2 \times 10^5$ m and $h_f = 800$ m,

Brought to you by HOKKAIDO DAIGAKU | Unauthenticated | Downloaded 05/13/26 12:03 AM UTC

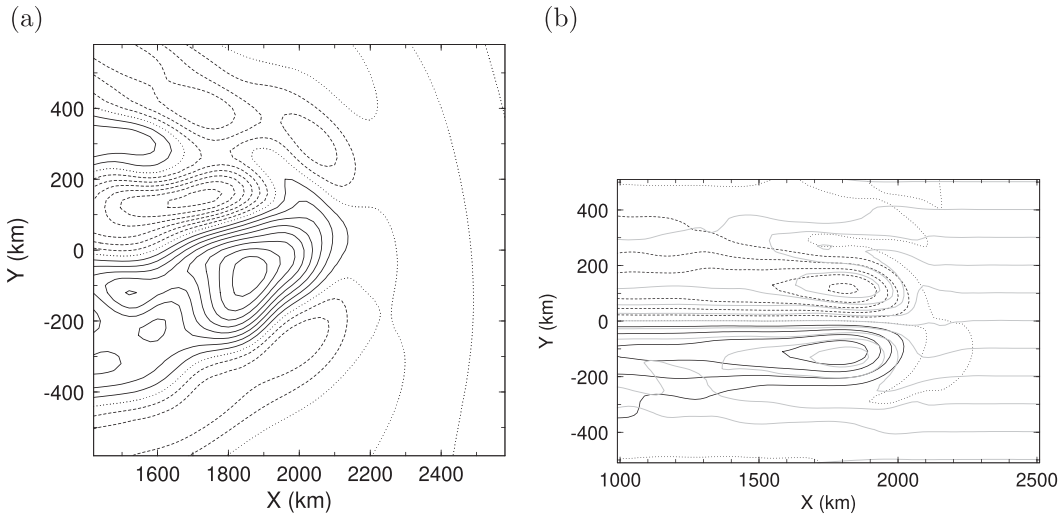


FIG. 18. Contours of the (a) snapshot geostrophic streamfunction at 4500 days and (b) mean geostrophic streamfunction in the surface layer in the finite-amplitude experiment. Contour intervals are 0.15 $m^2 s^{-2}$.

and the angular frequency of τ was $\omega = 2\pi \times 0.01$ rad day^{-1}. These values were determined from 1) the typical horizontal and vertical scales of the region in which the upgradient PV flux is large in the low-frequency bands and 2) the mean frequency of the low-frequency bands in section 3. We performed two experiments using A_f values of 5×10^{-3} and 0.15 $m^2 s^{-2}$, respectively. The former and latter are referred to as the small-amplitude and finite-amplitude experiments because typical values of the nondimensional parameter ϵ, which are estimated from results of the experiments, were 0.05 and 2, respectively. For comparison, the experiment analyzed in section 3 is referred to as the jet experiment. The dimensions of the model basin were 4000 and 3000 km in the x and y directions, respectively, and x_c in (28) was 2000 km. Other parameters were the same as those in the jet experiment.

We first examine the results of the small-amplitude experiment. Figures 14a–d show a snapshot of π, mean flow, upgradient PV flux, and the EE in the surface layer, respectively, which are directly obtained by the numerical model, in the small-amplitude experiment. Here, the surface layer is located at depths of ~400 m, as defined in section 2. The snapshot of π indicates that the barotropic Rossby wave is radiated from the forcing region, which is located at $(x, y) = (2000, 0)$ km (Fig. 14a). As shown by Haidvogel and Rhines (1983), the Rossby wave generates the upgradient PV flux and the mean flow, which are qualitatively similar to those in section 3, although the mean flow is weak (Figs. 14b,c). The EE, which is the source of the mean advection in (26), is concentrated near the forcing region (Fig. 14d).

Figure 15 compares each term in the equation of the EE [(24)] in the surface layer. Note that the contour intervals (CIs) are different between Figs. 15a–d. Because ϵ is small, the PUF is almost balanced by the external forcing (Figs. 15a,d). For comparison, Figs. 16 and 17 show each term predicted by (25) and (26), respectively. The external forcing coincides with that predicted by (25) (Figs. 15d and 16). The mean advection also coincides with that predicted by (26) (Figs. 15c and 17c). As we expect from the distribution of the EE (black contours) and mean geostrophic streamfunction (gray contours) in Fig. 14d, the mean advection is negative in the western part of the forcing region, $(x, y) = (1900, 0)$ km, where the mean flow is eastward and oriented in the upgradient direction of the EE (Fig. 15c). The mean advection is positive at $(x, y) = (2000, \pm 100)$ km, where the mean flow is oriented in the downgradient direction of the EE. The forced-wave interaction is also correctly predicted by (26) (Figs. 15b and 17b). The $O(\epsilon^2)$ components of the PUF (Fig. 17a) and external forcing (Fig. 17d) are not evident in the total field (Figs. 15a,d) because these terms are dominated by the $O(1)$ components.

Next, we examine the results of the finite-amplitude experiment, in which the amplitude of the Rossby wave is close to that in the jet experiment. Figures 18a and 18b show a snapshot of π and mean flow obtained by the finite-amplitude experiment. We can confirm that basic features of these quantities are similar to those obtained in the small-amplitude experiment, although π looks more irregular owing to the mean flow and higher-order waves. The maximum speed of the mean flow in the surface layer is ~5 cm and similar to that obtained in the jet experiment (not shown). Figure 19 shows each term in (24) in the surface layer. The external forcing (Fig. 19d) is positive in the forcing region as in the small-amplitude experiment (Fig. 15d). Moreover, the mean advection (Fig. 19c), which is two orders of magnitude smaller than the external forcing in the small-amplitude experiment, has an amplitude similar to that of the external forcing (Fig. 19d). Even if ϵ is not small, the distribution of the mean advection is qualitatively similar to that predicted by (26), which is shown in Fig. 17c, except that weakly negative regions exist at $y = \pm 200$ km. Thus, in contrast to the small-amplitude experiment, the PUF is balanced by both the external forcing and the mean advection in the finite-amplitude experiment. The forced-wave interaction is much smaller than the other terms (Fig. 19b). Thus, even if the mean flow is essentially driven by

Brought to you by HOKKAIDO DAIGAKU | Unauthenticated | Downloaded 05/13/26 12:03 AM UTC

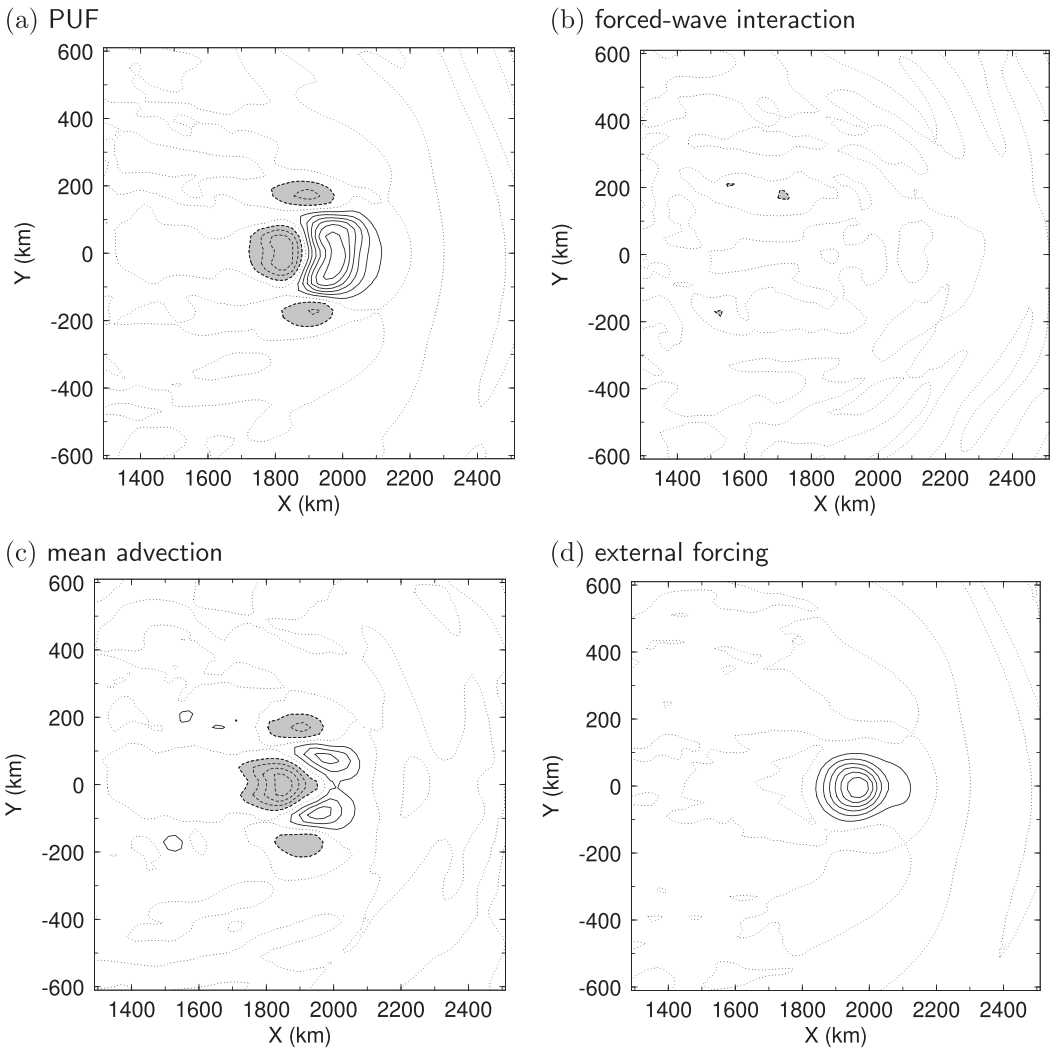


FIG. 19. Terms in the equation of the EE [(24)] for the finite-amplitude experiment in the surface layer. Contours of the (a) PUF, (b) forced-wave interaction, (c) mean advection, and (d) external forcing. Contour intervals are $2.5 \times 10^{-18}\ \mathrm{s}^{-3}$.

the Rossby wave, the mean advection can be as large as the eddy–eddy interaction, as shown in the jet experiment (Fig. 10). The mean advection has negative and positive values in the western and eastern parts near the forcing region, respectively. This distribution of the mean advection is broadly similar to that in the jet experiment in the low-frequency band (Fig. 10c), suggesting that the mean advection shown in Fig. 10c is produced by the wave-driven recirculation gyres.

5. Summary

To understand the driving mechanism of recirculation gyres, we examined the PV flux and enstrophy budget in an eastward jet. An upgradient eddy PV flux, which tends to drive the recirculation gyres, is generated near their eastern end, whereas a downgradient eddy PV flux is generated in the upstream region of the jet. These upgradient and downgradient PV fluxes are generated by perturbation in different frequency bands. The upgradient PV flux is generated by low-frequency perturbations, which are dominated by the Rossby wave. The downgradient PV flux is generated by high-frequency perturbations, which correspond to the instability wave of the jet.

The budget of the EE indicates that the PUF (i.e., the production/destruction of the EE by the downgradient/upgradient PV flux) is mainly balanced by the mean advection (i.e., advection of the EE by the mean flow) and the eddy–eddy interaction (i.e., the nonlinear interaction of different eddies). The mean advection seems to mostly balance the PUF. However, the eddy PV flux includes a large amount of the rotational component, which does not drive the mean flow. A large cancellation between the PUF and the mean advection is caused by this rotational component of the PV flux. Thus, as discussed by Holland and Rhines (1980), the PV flux tends to be oriented in the upgradient and downgradient directions of the mean PV in the

Brought to you by HOKKAIDO DAIGAKU | Unauthenticated | Downloaded 05/13/26 12:03 AM UTC

downstream and upstream parts of the jet, respectively. However, the PUF balanced by the mean advection is dominated by the production of the EE by the rotational component of the PV flux.

When the rotational component is subtracted, the PUF is nearly equally balanced by the eddy–eddy interaction as well as by the mean advection, indicating that the eddy forcing contributes to generating the upgradient PV flux. The PUF tends to be balanced by the eddy–eddy interaction in low-frequency bands in which the Rossby wave is dominant. Thus, the eddy forcing tends to excite the Rossby wave. In high-frequency bands, the EE is produced by jet instability in the upstream region. Advected to the downstream region, the EE is transferred from high- to low-frequency bands by the eddy–eddy interaction. Thus, the high-frequency perturbation produced by jet instability contributes in exciting the Rossby wave owing to the eddy–eddy interaction between perturbations. Most of the convergence and divergence of the eddy PV flux driving the recirculation gyres are generated by this Rossby wave radiation. These results are consistent with those obtained by previous studies (Hogg 1988; Malanotte-Rizzoli et al. 1995; Waterman and Jayne 2011).

Even after subtracting the rotational component, the amplitude of the mean advection is similar to that of the eddy–eddy interaction. To further examine the mechanism producing the mean advection, we considered an experiment in which the Rossby wave is excited by an external forcing as in Haidvogel and Rhines (1983). Assuming that the rotational component of the PV flux is mostly generated by the inflow and outflow from boundaries, we did not consider the inflow and outflow. Our results show that, in addition to the PUF associated with the Rossby wave radiation, the PUF can be balanced by the advection of the EE by the wave-driven mean flow. The amplitude of this PV flux generated by the advection becomes as large as that generated by the Rossby wave radiation when external forcing has finite amplitudes. These results are broadly consistent with those in the jet experiment, suggesting that the upgradient PV flux in the jet experiment is essentially generated by the Rossby wave radiation. Therefore, it is strongly suggested that the Rossby wave excited by the eddy–eddy interaction drives the recirculation gyres by generating the upgradient PV flux. These results are consistent with the mechanism proposed by Haidvogel and Rhines (1983), Waterman and Jayne (2011), and others.

In this study, we did not examine the vertical structure of the recirculation gyres or the physical process responsible for the eddy–eddy interaction, which transfers the EE from high- to low-frequency bands. We showed that the Rossby wave is excited by the eddy–eddy interaction in the surface layer. On the other hand, the eddy–eddy interaction in the deep layer is weaker, and the horizontal distribution is different compared to that in the surface layer (not shown). Thus, even if the Rossby wave excited by the eddy–eddy interaction is barotropic, the eddy PV flux in the deep layer is different from that in the surface layer, as shown by (1). Hence, the mechanism maintaining the deep recirculation gyres is still not clear. It is also not sufficiently clear how the westward-propagating Rossby wave is excited by the eastward-propagating instability wave. In the Kuroshio Extension, the transport, zonal extent, and latitude of the jet and recirculation gyres vary decadally (Qiu 2003; Qiu and Chen 2005). Clarifying the precise mechanism of the eddy–eddy interaction may significantly improve the understanding of the decadal variability of the Kuroshio Extension. These points are left for future research.

Acknowledgments. The present study was supported by JSPS KAKENHI Grant JP24K07128 and JP17K05649 and the Collaborative Research Program of the Research Institute for Applied Mechanics, Kyushu University.

Data availability statement. All data analyzed in this study are available at https://doi.org/10.5281/zenodo.15009688.

APPENDIX

Distribution of the Inflow, Outflow, and Stratification

We determined stratification and the vertical structure of the inflow and outflow by fitting the density near the Kuroshio Extension given in the *World Ocean Atlas 2005* (Locarnini et al. 2006; Antonov et al. 2006, https://www.nodc.noaa.gov/OC5/WOA05/pr_woa05.html) by a linear combination of exponential functions. Stratification was

$$\rho_s(z) = \rho_b - \frac{\rho_b}{g}[N_1^2 d_1(e^{z/d_1} - 1) + N_2^2 d_2(e^{z/d_2} - 1) + N_3^2 d_3(e^{z/d_3} - 1)], \tag{A1}$$

in a state of rest. Here, the Boussinesq density ρ_b was 1025 kg m^{-3}, and the gravity acceleration g was 9.81 m s^{-2}. Other parameters were $d_0 = 750$ m, $d_1 = 1800$ m, $d_2 = 400$ m, $d_3 = 200$ m, $N_1^2 = 3.14 \times 10^{-6}$ s^{-2}, $N_2^2 = 8.90 \times 10^{-5}$ s^{-2}, and $N_3^2 = -9.17 \times 10^{-5}$ s^{-2}. The distribution of the inflow and outflow was

$$u_{\text{in}}(y, z) = \frac{u_0 f_0 (2d_0 e^{z/d_0} - d_3 e^{z/d_3})}{f(2d_0 - d_3)\cosh^2 \dfrac{y}{L_{\text{in}}}} \tag{A2}$$

and

$$u_{\text{out}}(y, z) = \frac{u_1 f_0 (2d_0 e^{z/d_0} - d_3 e^{z/d_3})}{f(2d_0 - d_3)}, \tag{A3}$$

respectively, where $f = f_0 + \beta y$ is the Coriolis parameter. The value of u_1 was numerically determined so that the transport of the inflow is balanced by that of the outflow.

From (A2) and (A3), and the geostrophic balance, the pressure of the inflow and outflow was

$$p_{\text{in}}(y, z) = -\frac{\rho_b u_0 f_0 L_{\text{in}} (2d_0 e^{z/d_0} - d_3 e^{z/d_3}) \tanh \dfrac{y}{L_{\text{in}}}}{2d_0 - d_3} \tag{A4}$$

and

$$p_{\text{out}}(y, z) = -\frac{\rho_b u_1 f_0 (2d_0 e^{z/d_0} - d_3 e^{z/d_3}) y}{2d_0 - d_3}, \tag{A5}$$

respectively. We determined the surface elevation and the perturbation of density from $\rho_s(z)$ by using (A4) and (A5) and the hydrostatic balance.

Brought to you by HOKKAIDO DAIGAKU | Unauthenticated | Downloaded 05/13/26 12:03 AM UTC

REFERENCES

Antonov, J. I., R. A. Locarnini, T. P. Boyer, A. V. Mishonov, and H. E. Garcia, 2006: *Salinity*. Vol. **2**, *World Ocean Atlas 2005*, NOAA Atlas NESDIS 62, 182 pp.

Aoki, K., S. Minobe, Y. Tanimoto, and Y. Sasai, 2013: Southward eddy heat transport occurring along southern flanks of the Kuroshio Extension and the Gulf Stream in a 1/10° global ocean general circulation model. *J. Phys. Oceanogr.*, **43**, 1899–1910, https://doi.org/10.1175/JPO-D-12-0223.1.

——, A. Kubokawa, R. Furue, and H. Sasaki, 2016: Influence of eddy momentum fluxes on the mean flow of the Kuroshio Extension in a 1/10° ocean general circulation model. *J. Phys. Oceanogr.*, **46**, 2769–2784, https://doi.org/10.1175/JPO-D-16-0021.1.

Berloff, P., 2015: Dynamically consistent parameterization of mesoscale eddies. Part I: Simple model. *Ocean Modell.*, **87**, 1–19, https://doi.org/10.1016/j.ocemod.2014.12.008.

Bower, A. S., and N. G. Hogg, 1992: Evidence for barotropic wave radiation from the Gulf Stream. *J. Phys. Oceanogr.*, **22**, 42–61, https://doi.org/10.1175/1520-0485(1992)022<0042:EFBWRF>2.0.CO;2.

Cessi, P., G. Ierley, and W. Young, 1987: A model of the inertial recirculation driven by potential vorticity anomalies. *J. Phys. Oceanogr.*, **17**, 1640–1652, https://doi.org/10.1175/1520-0485(1987)017<1640:AMOTIR>2.0.CO;2.

Chen, R., G. R. Flierl, and C. Wunsch, 2014: A description of local and nonlocal eddy–mean flow interaction in a global eddy-permitting state estimate. *J. Phys. Oceanogr.*, **44**, 2336–2352, https://doi.org/10.1175/JPO-D-14-0009.1.

Emery, W. J., and R. E. Thomson, 2001: *Data Analysis Methods in Physical Oceanography*. Elsevier Science, 638 pp.

Haidvogel, D. B., and P. B. Rhines, 1983: Waves and circulation driven by oscillatory winds in an idealized ocean basin. *Geophys. Astrophys. Fluid Dyn.*, **25** (1–2), 1–63, https://doi.org/10.1080/03091928308221747.

——, J. C. McWilliams, and P. R. Gent, 1992: Boundary current separation in a quasigeostrophic, eddy-resolving ocean circulation model. *J. Phys. Oceanogr.*, **22**, 882–902, https://doi.org/10.1175/1520-0485(1992)022<0882:BCSIAQ>2.0.CO;2.

——, H. G. Arango, K. Hedstrom, A. Beckmann, P. Malanotte-Rizzoli, and A. F. Shchepetkin, 2000: Model evaluation experiments in the North Atlantic Basin: Simulations in nonlinear terrain-following coordinates. *Dyn. Atmos. Oceans*, **32**, 239–281, https://doi.org/10.1016/S0377-0265(00)00049-X.

Hogg, N. G., 1983: A note on the deep circulation of the western North Atlantic: Its nature and causes. *Deep-Sea. Res.*, **30A**, 945–961, https://doi.org/10.1016/0198-0149(83)90050-X.

——, 1988: Stochastic wave radiation by the Gulf Stream. *J. Phys. Oceanogr.*, **18**, 1687–1701, https://doi.org/10.1175/1520-0485(1988)018<1687:SWRBTG>2.0.CO;2.

——, 1992: On the transport of the Gulf Stream between Cape Hatteras and the Grand Banks. *Deep-Sea. Res.*, **39A**, 1231–1246, https://doi.org/10.1016/0198-0149(92)90066-3.

Holland, W. R., and P. B. Rhines, 1980: An example of eddy-induced ocean circulation. *J. Phys. Oceanogr.*, **10**, 1010–1031, https://doi.org/10.1175/1520-0485(1980)010<1010:AEOEIO>2.0.CO;2.

Imawaki, S., H. Uchida, Y.-X. Qiao, and H. Nakamura, 2025: Kuroshio volume transport over the past 3 decades estimated from combined satellite altimetry and hydrography data. *J. Oceanogr.*, **81**, 351–359, https://doi.org/10.1007/s10872-025-00756-w.

Jayne, S. R., and J. Marotzke, 2002: The oceanic eddy heat transport. *J. Phys. Oceanogr.*, **32**, 3328–3345, https://doi.org/10.1175/1520-0485(2002)032<3328:TOEHT>2.0.CO;2.

——, N. G. Hogg, and P. Malanotte-Rizzoli, 1996: Recirculation gyres forced by a beta-plane jet. *J. Phys. Oceanogr.*, **26**, 492–504, https://doi.org/10.1175/1520-0485(1996)026<0492:RGFBAB>2.0.CO;2.

——, and Coauthors, 2009: The Kuroshio Extension and its recirculation gyres. *Deep-Sea. Res. I*, **56**, 2088–2099, https://doi.org/10.1016/j.dsr.2009.08.006.

Kawai, H., 1972: Hydrography of the Kuroshio Extension. *Its Physical Aspects*, H. Stommel, and K. Yoshida, Eds., University of Tokyo Press, 235–354.

Lau, N.-C., and J. M. Wallace, 1979: On the distribution of horizontal transports by transient eddies in the Northern Hemisphere wintertime circulation'. *J. Atmos. Sci.*, **36**, 1844–1861, https://doi.org/10.1175/1520-0469(1979)036<1844:OTDOHT>2.0.CO;2.

Locarnini, R. A., A. V. Mishonov, J. I. Antonov, T. P. Boyer, and H. E. Garcia, 2006: *Temperature*. Vol. **1**, *World Ocean Atlas 2005*, NOAA Atlas NESDIS 61, 182 pp.

Malanotte-Rizzoli, P., N. G. Hogg, and R. E. Young, 1995: Stochastic wave radiation by the Gulf Stream: Numerical experiments. *Deep-Sea. Res. I*, **42**, 389–423, https://doi.org/10.1016/0967-0637(95)00001-M.

Marshall, J. C., 1984: Eddy-mean-flow interaction in a barotropic ocean model. *Quart. J. Roy. Meteor. Soc.*, **110**, 573–590, https://doi.org/10.1002/qj.49711046502.

——, and G. Shutts, 1981: A note on rotational and divergent eddy fluxes. *J. Phys. Oceanogr.*, **11**, 1677–1680, https://doi.org/10.1175/1520-0485(1981)011<1677:ANORAD>2.0.CO;2.

Matsuta, T., and Y. Masumoto, 2021: Modified view of energy budget diagram and its application to the Kuroshio Extension region. *J. Phys. Oceanogr.*, **51**, 1163–1175, https://doi.org/10.1175/JPO-D-20-0124.1.

Mizuta, G., 2009: Rossby wave radiation from an eastward jet and its recirculations. *J. Mar. Res.*, **67**, 185–212, https://doi.org/10.1357/002224009789051227.

——, 2018: Upgradient and downgradient potential vorticity fluxes produced by forced Rossby waves. Part I: Basic experiments. *J. Phys. Oceanogr.*, **48**, 1191–1209, https://doi.org/10.1175/JPO-D-17-0197.1.

Nakano, H., H. Tsujino, and R. Furue, 2008: The Kuroshio Current System as a jet and twin "relative" recirculation gyres embedded in the Sverdrup circulation. *Dyn. Atmos. Oceans*, **45**, 135–164, https://doi.org/10.1016/j.dynatmoce.2007.09.002.

Oka, E., K. Yamada, D. Sasano, K. Enyo, T. Nakano, and M. Ishii, 2019: Remotely forced decadal physical and biogeochemical variability of North Pacific Subtropical Mode Water over the last 40 years. *Geophys. Res. Lett.*, **46**, 1555–1561, https://doi.org/10.1029/2018GL081330.

Qiu, B., 2003: Kuroshio Extension variability and forcing of the Pacific decadal oscillations: Responses and potential feedback. *J. Phys. Oceanogr.*, **33**, 2465–2482, https://doi.org/10.1175/2459.1.

——, and S. Chen, 2005: Variability of the Kuroshio Extension jet, recirculation gyre, and mesoscale eddies on decadal time scales. *J. Phys. Oceanogr.*, **35**, 2090–2103, https://doi.org/10.1175/JPO2807.1.

——, and ——, 2006: Decadal variability in the formation of the North Pacific Subtropical Mode Water: Oceanic versus atmospheric control. *J. Phys. Oceanogr.*, **36**, 1365–1380, https://doi.org/10.1175/JPO2918.1.

——, and ——, 2011: Effect of decadal Kuroshio Extension jet and eddy variability on the modification of North Pacific

Brought to you by HOKKAIDO DAIGAKU | Unauthenticated | Downloaded 05/13/26 12:03 AM UTC

Intermediate Water. *J. Phys. Oceanogr.*, **41**, 503–515, https://doi.org/10.1175/2010JPO4575.1.

Rhines, P. B., and W. R. Holland, 1979: A theoretical discussion of eddy-driven mean flows. *Dyn. Atmos. Oceans*, **3**, 289–325, https://doi.org/10.1016/0377-0265(79)90015-0.

——, and W. R. Young, 1982a: Homogenization of potential vorticity in planetary gyres. *J. Fluid Mech.*, **122**, 347–367, https://doi.org/10.1017/S0022112082002250.

——, and ——, 1982b: A theory of wind-driven circulation. I. mid-ocean gyres. *J. Mar. Res.*, **40**, 559–596.

Sheremet, V. A., 2002: Inertial gyre driven by a zonal jet emerging from the western boundary. *J. Phys. Oceanogr.*, **32**, 2361–2378, https://doi.org/10.1175/1520-0485(2002)032<2361:IGDBAZ>2.0.CO;2.

Taguchi, B., S.-P. Xie, H. Mitsudera, and A. Kubokawa, 2005: Response of the Kuroshio Extension to Rossby waves associated with the 1970s climate regime shift in a high-resolution ocean model. *J. Climate*, **18**, 2979–2995, https://doi.org/10.1175/JCLI3449.1.

——, B. Qiu, M. Nonaka, H. Sasaki, S.-P. Xie, and N. Schneider, 2010: Decadal variability of the Kuroshio Extension: Mesoscale eddies and recirculations. *Ocean Dyn.*, **60**, 673–691, https://doi.org/10.1007/s10236-010-0295-1.

Thompson, R. O. R. Y., 1977: Observations of Rossby waves near site D[1]. *Prog. Oceanogr.*, **7**, 135–162, https://doi.org/10.1016/0079-6611(77)90003-9.

Vallis, G. K., 2006: *Atmosphere and Oceanic Fluid Dynamics.* Cambridge University Press, 745 pp.

Wallace, J. M., and R. E. Dickinson, 1972: Empirical orthogonal representation of time series in the frequency domain. Part I: Theoretical considerations. *J. Appl. Meteor.*, **11**, 887–892, https://doi.org/10.1175/1520-0450(1972)011<0887:EOROTS>2.0.CO;2.

Waterman, S., and S. R. Jayne, 2011: Eddy-mean flow interactions in the along-stream development of a western boundary current jet: An idealized model study. *J. Phys. Oceanogr.*, **41**, 682–707, https://doi.org/10.1175/2010JPO4477.1.

Wilson, C., and R. G. Williams, 2004: Why are eddy fluxes of potential vorticity difficult to parameterize? *J. Phys. Oceanogr.*, **34**, 142–155, https://doi.org/10.1175/1520-0485(2004)034<0142:WAEFOP>2.0.CO;2.

Worthington, L. V., 1976: *On the North Atlantic Circulation.* Vol. 6. The Johns Hopkins University Press, 110 pp.

Brought to you by HOKKAIDO DAIGAKU | Unauthenticated | Downloaded 05/13/26 12:03 AM UTC